J. Fluid Mech. (2006), *vol.* 546, *pp.* 395–432. © 2005 Cambridge University Press
doi:10.1017/S0022112005007275 Printed in the United Kingdom

Instabilities in boundary-layer flows on a curved surface

By OLEG S. RYZHOV[1] AND ELENA V. BOGDANOVA-RYZHOVA[2]

[1]Department of Mechanical and Aeronautical Engineering, University of California Davis, Davis, CA 95616, USA

[2]GE Global Research Center, Fluid Mechanics Laboratory, Schenectady, NY 12305, USA

(Received 16 February 2004 and in revised form 21 March 2005)

Recent theoretical findings show that the curvature of streamsurfaces naturally warping in the crossflow direction of a three-dimensional boundary layer can maintain centrifugal forces, provoking unsteady short-scaled vortices. The wave/vortex eigenmode coupling takes place in the linear stage of disturbance evolution and results in streamwise absolute instability. The two-dimensional flow past a curved cylindrical surface under consideration here provides an example where centrifugal forces are associated with the fixed curvature of a solid wall bending in the direction of the main stream. The spiral-type Görtler vortices develop in proximity to the surface and their interaction with the Tollmien–Schlichting eigenmodes creates a mechanism driving disturbances both downstream and upstream of a perturbing agency. The vortex eigenmodes arising from centrifugal forces are balanced out by the normal-to-wall pressure gradient. Some higher-order terms need to be kept in its expansion to achieve the modal coupling. As a consequence, a side band appears in the spectra of eigen-frequencies and wavenumbers featuring the classical triple-deck scheme. The extended composite asymptotic model proves to be self-consistent, with the Cauchy problem well-posed in the limit of large Reynolds numbers. It follows from the extended model that the boundary layer on a concave surface, much like the one with crossflow, suffers absolute instability in the streamwise direction. This unusual property may lead to earlier transition or, conversely, be exploited to artificially excite the nonlinear vortex structures with delayed transition.

1. Introduction

The Görtler instability of flow past a concave solid surface has profound similarities to that occurring in a fluid under the action of dynamical effects of rotation. Rayleigh (1880, 1916) was the first to study a base inviscid swirling flow endowed with angular velocity $\overline{\Omega} = \overline{\Omega}(\bar{r})$ which can vary in an arbitrary way with the distance $\bar{r}$ from the rotation axis. By a simple physical reasoning, he arrived at the conclusion that a necessary and sufficient condition for stability to axisymmetric disturbances takes the form

$$\overline{R}(\bar{r}) = \frac{1}{\bar{r}^3}\frac{\mathrm{d}}{\mathrm{d}\bar{r}}(\bar{r}^2\overline{\Omega})^2 \geqslant 0 \tag{1.1}$$

everywhere in the flow field. The overbars in (1.1) and below are used to designate non-dimensional quantities. The stability of viscous fluid in a gap between two coaxial cylinders has been widely investigated. In particular, Taylor (1921) showed that the

https://doi.org/10.1017/S0022112005007275 Published online by Cambridge University Press

motion emerging at the onset of instability is axisymmetric, in full accord with the assumption by Rayleigh (1880, 1916). But more importantly, (1.1) proved to break down if the cylinders rotated in the opposite directions. Hence it became clear that viscosity plays a crucial role in stability of rotating fluid. Vortical disturbances in a flow between two cylinders were further examined, theoretically as well as experimentally, in remarkable papers by Taylor (1923, 1935). This work led him to the discovery of centrifugal instability acted upon by viscous effects.

Görtler (1940) extended the study of centrifugal instability to boundary layers on concave surfaces. Analogous conditions are realized according to subsequent work by Görtler (1955) in the vicinity of the stagnation point on the blunted nose of a body. The same is true with regard to concave streamlines in the region where a separated shear layer reattaches to a solid surface. However, as will be shown in the present paper, the curvature of naturally bending streamlines does not act in the same way as the fixed curvature of a solid surface. Vortical disturbances typical of this type of boundary-layer instability are referred to as Görtler vortices. As usual, the Görtler number

$$G\ddot{o} = \frac{1}{|\overline{R}_s|^{1/2}} Re = Re\,|\overline{\kappa}|^{1/2} \tag{1.2}$$

is introduced to determine their structure. Here $\overline{\kappa}$ and $\overline{R}_s$ are the local curvature of a body and the radius of curvature, respectively; Re denotes the Reynolds number. In contrast to Tollmien–Schlichting waves, the Görtler vortices were assumed in earlier investigations to be standing disturbances. Those investigations encouraged a great many attempts to resolve the centrifugal viscous instability problem both theoretically and experimentally. The linear asymptotic analysis by Hall (1982) applies to the vortex development in space, whereas in Hall (1983) allowance is made for the boundary-layer growth in the downstream direction. Further results in the framework of a time-independent approach are available in Hall (1990), Floryan (1991) and Saric (1994).

In the wake of the pioneering work by Taylor (1921, 1923, 1935) more complicated swirling waves superimposed on the primary stationary disturbances have been observed in the fluid motion in a gap between two cylinders. Their time-dependent counterparts are also present in boundary-layer flows. However, the spatial open-flow properties of the Görtler problem make it unique. It does not share the intricate bifurcations intrinsic to the Taylor problem (Coles 1965). Nevertheless Timoshin (1990), Denier, Hall & Seddougui (1991) and Choudhari, Hall & Streett (1994) identified five different asymptotic regimes in the limit of large Görtler numbers, depending on the non-dimensional wavelength λ_z in the spanwise direction. If the surface curvature $\overline{\kappa} = O(1)$, then this limit is equivalent by virtue of (1.2) to the assumption that $Re \to \infty$. One of these five regimes (the long-wavelength one in terms of λ_z) is based on viscous/inviscid interaction of the triple-deck type considered in more detail below. It will be addressed to shed light on the crucial impact of centrifugal forces on the process of disturbance amplification, provoking a new type of instability.

The growth of stationary Görtler vortices is governed by the linear centrifugal instability up to a point where a strong nonlinear rearrangement of the velocity field occurs. Then travelling-wave-type disturbances in the form of sinuous and varicose secondary eigenmodes come into play. According to Li & Malik (1995) and Bottaro & Klingmann (1996) it is precisely these secondary instabilities which cause the laminar boundary layer on a concave wall to break down at some stage prior to transition.

https://doi.org/10.1017/S0022112005007275 Published online by Cambridge University Press

To place the current work into context, earlier asymptotic studies on wave/vortex interactions by Hall & Smith (1988, 1989, 1991), Smith & Walton (1989) and Walton & Simth (1992) are worthy of mention. They are not confined to weakly nonlinear disturbances but focus on truly nonlinear amplification mechanisms. According to Hall & Smith (1988, 1989, 1991), in strong interactions the surface curvature is not required at all to sustain longitudinal vortex structures essentially identical to Görtler vortices. The secondary instability properties are known to be in general different from those featuring the primary linear instability. In fact, all secondary instabilities discovered so far in the boundary layer with crossflow are of convective nature (Koch 2002; Wassermann & Kloker 2002; Saric, Reed & White 2003). One may infer from this that the streamwise absolute instability of primary crossflow vortices does not necessarily lead to earlier transition.

The aforementioned stationary regime controlled by the triple-deck disturbance pattern first appeared in Rozhko & Ruban (1987) where it was referred to as criss-cross interaction. The governing equations were applied by Rozhko, Ruban & Timoshin (1988) to the boundary layer on a body with an elongated obstacle placed on its curved surface. In this earlier work the process of criss-cross interaction was not identified with the formation of Görtler vortices. The fact that both mechanisms are inextricably entwined became clear from the analysis by Timoshin (1990) and Denier *et al.* (1991). With time-dependence included, Ruban (1990*a*, *b*) tackled the receptivity problem on the wave packet emitted by a vibrator operating in the pulse mode. Four years later Choudhari *et al.* (1994) came up with a different approach to solving the problem. Singular asymptotic expansions embracing both Tollmien–Schlichting waves and the unsteady spiral-type Görtler vortices were briefly discussed by Ryzhov (2003) and Ryzhov & Bogdanova-Ryzhova (2003). In an extended triple-deck model, the Görtler vortices give rise to a side band in the Tollmien–Schlichting spectrum of eigen-frequencies and wavenumbers. The coupling of wave and vortical eigenmodes brings about a dramatic change in the boundary-layer properties that results in absolute instability in the streamwise direction. Unlike the convective instability provoked by disturbances sweeping downstream from a site where they were excited, in this scenario of transition the highly modulated wave packets are capable of advancing upstream of a generator operating in the pulse mode. Hence the group velocity of signals appears in place of the phase velocity of monochromatic Tollmien–Schlichting wave trains. An analogous effect has been discovered by Lingwood (1997) and Ryzhov & Terent'ev (1998) in their studies of a three-dimensional boundary layer with crossflow. In either case, a small parameter depending on the Reynolds number and incorporating some other quantities such as skin friction and characteristic temperatures enters the dispersion relation typical of the eigenmode coupling regime. A particular value of this parameter determines the time/space scaling of side-band oscillations responsible for absolute instability of the boundary layer whether it be two-dimensional in the unperturbed state or three-dimensional from the very beginning owing to the presence of crossflow. A strong singularity appearing in the dispersion relation underlies a remarkable mathematical analogy between the two types of vortical disturbances. It is this singularity which underlies the mechanism driving wave packets upstream, against the oncoming boundary layer.

Our concern is mainly with the fundamental physical processes that take place in the viscous near-wall sublayer. A composite asymptotic model of the triple-deck type is advanced to provide a unified treatment of oscillations in the Tollmien–Schlichting interval of frequencies and wavenumbers as well as vortical eigenmodes from the

https://doi.org/10.1017/S0022112005007275 Published online by Cambridge University Press

spectral side band. Alterations introduced to the interaction law relating the self-induced pressure to the instantaneous displacement thickness are the cornerstone of the asymptotic model. On the assumption that the local Reynolds number Re is large enough, the contribution from centrifugal forces to the normal-to-wall pressure gradient proves to be $O(\varepsilon^3)$ within the Tollmien–Schlichting wave range, where $\varepsilon = Re^{-1/8}$ in accord with the conventional version of the triple-deck theory. However, the correction term becomes comparable with the leading-order one provided that the spiral-type Görtler vortices determine the disturbance pattern scaled in terms of the spectral side band.

The local Reynolds number Re is based on a reference length L^* associated with a specific point on a concave cylindrical surface, the free-stream velocity U_∞^*, density ρ_∞^* and viscosity μ_∞^* just outside the boundary layer. Only subsonic flows are under consideration, so the Mach number $M_\infty < 1$. The time $\bar{t}$ and spatial orthogonal curvilinear coordinates $(\bar{x}, \bar{y}, \bar{z})$ are non-dimensionalized with respect to L^*/U_∞^* and L^*, respectively; the $\bar{x}$-axis is aligned with the direction of the local main stream, $\bar{y}$ stands for the normal-to-wall distance and $\bar{z}$ defines the spanwise direction of the surface generators. The corresponding non-dimensional velocities are based on U_∞^*, and the streamwise velocity profile $U_0(y_2)$, where $\bar{y} = Re^{-1/2} y_2$, specifies the boundary-layer properties. Given that a ratio μ^*/μ_∞^* of viscosities is expressed in terms of a ratio T^*/T_∞^* of temperatures by the Chapman linear law $\mu^*/\mu_\infty^* = CT^*/T_\infty^*$, the normalized wall shear stress is

$$\tau_w = C^{1/2} \frac{T_w^*}{T_\infty^*} \frac{\mathrm{d}U_0(0)}{\mathrm{d}y_2} \tag{1.3}$$

The density $\bar{\rho}$ and excess pressure $\bar{p}$ are non-dimensionalized with respect to ρ_∞^* and $\rho_\infty^* U_\infty^{*2}$, respectively, and $R_0(y_2)$ denotes the density profile in the original boundary layer. For an insulated surface $\mathrm{d}R_0(0)/\mathrm{d}y_2 = 0$, but if the heat flux occurs across the surface then $\mathrm{d}R_0(0)/\mathrm{d}y_2 \neq 0$. Mathematical descriptions of these two regimes are quite different (Stewartson 1974).

2. Curvature-related pressure

In order to ascertain how strongly the surface curvature can affect the spectral parameters of Tollmien–Schlichting waves, higher-order expansions need to be introduced in the conventional triple-deck scheme. However, as consideration of space prevents us from thoroughly expounding the general theory, only terms responsible for the curvature effects underlying the boundary-layer structure in the original and perturbed states will be treated in detail.

Asymptotic expansions

To elucidate this issue of conceptual significance, let us begin with a discussion of asymptotic expansions

$$\bar{u} = U_0(y_2) + \varepsilon u_{21} + \varepsilon^2 u_{22} + \varepsilon^3 u_{23} + \varepsilon^4 u_{24} + \cdots, \tag{2.1a}$$

$$\bar{v} = \varepsilon^2 v_{21} + \varepsilon^3 v_{22} + \varepsilon^4 v_{23} + \varepsilon^5 v_{24} + \cdots, \tag{2.1b}$$

$$\bar{w} = \varepsilon^2 w_{21} + \varepsilon^3 w_{22} + \varepsilon^4 w_{23} + \varepsilon^5 w_{24} + \cdots, \tag{2.1c}$$

$$\bar{p} = \varepsilon^2 p_{21} + \varepsilon^3 p_{22} + \varepsilon^4 p_{23} + \varepsilon^5 p_{24} + \cdots, \tag{2.1d}$$

$$\bar{\rho} = R_0(y_2) + \varepsilon \rho_{21} + \varepsilon^2 \rho_{22} + \varepsilon^3 \rho_{23} + \varepsilon^4 \rho_{24} + \cdots, \tag{2.1e}$$

written in powers of ε for the main deck embracing most of the boundary layer. Here all the desired functions depend on scaled variables t_c, x_c, y_2, z_c of the compressible

https://doi.org/10.1017/S0022112005007275 Published online by Cambridge University Press

triple deck which are defined through (Stewartson 1974; Smith 1982)

$$\bar{t} = \varepsilon^2 t_c, \tag{2.2a}$$

$$\bar{x} = 1 + \varepsilon^3 x_c, \tag{2.2b}$$

$$\bar{y} = \varepsilon^4 y_2, \tag{2.2c}$$

$$\bar{z} = \varepsilon^3 z_c. \tag{2.2d}$$

The first number, 2, in the subscripts relates to the main deck sandwiched between the external, essentially inviscid, sublayer and the viscous near-wall sublayer. These two are labelled 1 and 3 below, respectively. Within the framework of the classical theory by Prandtl the normal-to-wall pressure gradient

$$\frac{\partial \bar{p}_2}{\partial y_2} = -\bar{\kappa}\frac{\bar{\rho}_2 \bar{u}_2^2}{Re^{1/2}} \tag{2.3}$$

expressed in terms of density $\bar{\rho}_2$ and streamwise velocity $\bar{u}_2$ becomes as large as $O(Re^{-1/2})$ across the boundary layer provided that the curvature of the solid surface does not vanish to zero. That implies the emergence of $O(\varepsilon^3)$ terms in expansions (2.1*a*) and (2.1*e*) for the streamwise velocity and density as well as $O(\varepsilon^4)$ terms in expansions (2.1*b*, *c*) for the transverse and lateral components of velocity which are provoked by an $O(\varepsilon^4)$ term in expansion (2.1*d*) for the pressure. Most important of all, the terms mentioned relate to the base steady flow rather than the perturbations generated in the base flow. On the other hand, the terms induced by Tollmien–Schlichting waves are of lower order in magnitude. Hence we are led to conclude that the third-order correction terms need to be included in the triple deck for taking into account the base steady flow on a curved surface, while the fourth-order correction terms come into play when considering the impact of the surface curvature on the spectral properties of the boundary-layer eigenmodes.

A comment on the form of asymptotic expansions is due at this point. They are assumed in (2.1*a–e*) to proceed in powers of ε. However there are two sources giving rise to powers of $\log\varepsilon$ in the desired solution. One of them stems from the logarithmic behaviour of the velocity and density fields in most of the boundary layer as the Prandtl variable $y_2 \to 0$ if the wall is kept at an arbitrary temperature (Stewartson 1974). The second source of the higher-order terms in powers of $\log\varepsilon$ originates from the logarithmic singularity entering the main-deck expansion for the normal-to-wall velocity as $y_2 \to 0$. Smith (1979) pointed out a technique to accommodate the logarithmic singularity as applied to the incompressible Blasius boundary layer slowly thickening in the streamwise direction. Since the non-parallel flow corrections bear no relation to the problem where the normal-to-wall pressure gradient strikes a balance with centrifugal forces maintained by the surface curvatures, the logarithmic terms are not included into (2.1*a–e*).

Base steady flow

In the vicinity of any point of interest the surface can be approximated with an accuracy sufficient for our purposes by a circular cylinder of non-dimensional radius $\bar{R}_s$. Inside the steady boundary layer, the pressure is expanded as

$$\bar{p}_2 = \bar{p}_{s0}(\bar{x}) + Re^{-1/2}\bar{p}_{21}^{(\kappa)}(\bar{x}, y_2) + \cdots$$

where $\bar{p}_{s0}(\bar{x})$ is the distribution over the solid surface that comes from an external flow solution, and $\bar{p}_{21}^{(\kappa)}$ designates the contribution induced by the surface curvature $\bar{\kappa} = -1/\bar{R}_s$. The same superscript will be used to label other functions arising from

https://doi.org/10.1017/S0022112005007275 Published online by Cambridge University Press

the curvature effects. It follows from (2.3) that $\overline{p}_{21}^{(\kappa)}$ obeys an equation

$$\frac{\partial \overline{p}_{21}^{(\kappa)}}{\partial y_2} = -\overline{\kappa}\,\overline{\rho}_{20}\overline{u}_{20}^2 \tag{2.4}$$

and can be found in an explicit form.

Self-induced pressure

The next term in the asymptotic expansion (2.1*d*) derives from the self-induced pressure $p_{24}^{(\kappa)}$ of eigenmodes affected by centrifugal forces. At this point, (2.3) is invoked again to give

$$\frac{\partial p_{24}^{(\kappa)}}{\partial y_2} = -\overline{\kappa}\left(2R_0U_0u_{21} + U_0^2\rho_{21}\right) \tag{2.5}$$

in the scaled triple-deck variables t_c, x_c, y_2, z_c introduced by (2.2*a–d*). As (2.5) shows, only the first-order velocity and density fields are necessary to evaluate the fourth-order pressure striking a balance with centrifugal forces. A complete first-order solution is available in Stewartson (1974), Smith, Sykes & Brighton (1977) Ryzhov (1980) and Smith (1982). It can be written as

$$u_{21} = A_1(t_c, x_c, z_c)\frac{\mathrm{d}U_0}{\mathrm{d}y_2}, \tag{2.6a}$$

$$v_{21} = -\frac{\partial A_1}{\partial x_c}U_0(y_2), \tag{2.6b}$$

$$R_0(y_2)\,U_0(y_2)\frac{\partial w_{21}}{\partial x_c} + \frac{\partial p_{21}}{\partial z_c} = 0, \tag{2.6c}$$

$$p_{21} = p_{21}(t_c, x_c, z_c), \tag{2.6d}$$

$$\rho_{21} = A_1(t_c, x_c, z_c)\frac{\mathrm{d}R_0}{\mathrm{d}y_2} \tag{2.6e}$$

in terms of the instantaneous displacement thickness $-A_1(t_c, x_c, z_c)$. Inserting u_{21} and ρ_{21} from (2.6*a*) and (2.6*e*), respectively, in (2.5) results in

$$p_{24}^{(\kappa)} = p_{24}^{(\kappa)}(t_c, x_c, 0, z_c) - \overline{\kappa}R_0(y_2)\,U_0^2(y_2)\,A_1(t_c, x_c, z_c). \tag{2.7}$$

It should be emphasized that $p_{24}^{(\kappa)}$ represents only a part of the self-induced pressure caused by centrifugal forces in the boundary layer on a curved surface; the other contributions to p_{24} from the higher-order terms entering the asymptotic expansions (2.1*a–e*) are dropped, as they do not bring new physics into the problem posed. If necessary, the contributions mentioned can be accounted for separately since all of them are generated by independent linear processes.

With the above results in hand, the asymptotic expansion (2.1*d*) for the pressure reduces to

$$\overline{p} = \varepsilon^2 p_{21} + \varepsilon^3 p_{22} + \varepsilon^4 p_{23}^{(\kappa)} + \cdots + \varepsilon^5 p_{24}^{(\kappa)} + \cdots \tag{2.8}$$

allowing us to study conceptually new destabilizing effects caused by swirling waves in the boundary layer on a concave surface. On the assumption that $M_\infty < 1$, expressions for the first two terms coming from the matching with the outer inviscid flow are presented in Stewartson (1974), Smith *et al.* (1977), Ryzhov (1980) and Smith (1982).

https://doi.org/10.1017/S0022112005007275 Published online by Cambridge University Press

Asymptotic expansions in the upper deck labelled 1 can be written in the form

$$\begin{aligned}
\overline{u} &= 1 + \varepsilon^2 u_{11} + \varepsilon^3 u_{12} + \varepsilon^4 u_{13} + \varepsilon^5 u_{14} + \cdots,\\
\overline{v} &= \varepsilon^2 v_{11} + \varepsilon^3 v_{12} + \varepsilon^4 v_{13} + \varepsilon^5 v_{14} + \cdots,\\
\overline{w} &= \varepsilon^2 w_{11} + \varepsilon^3 w_{12} + \varepsilon^4 w_{13} + \varepsilon^5 w_{14} + \cdots,\\
\overline{p} &= \varepsilon^2 p_{11} + \varepsilon^3 p_{12} + \varepsilon^4 p_{13} + \varepsilon^5 p_{14} + \cdots,\\
\overline{\rho} &= 1 + \varepsilon^2 \rho_{11} + \varepsilon^3 \rho_{12} + \varepsilon^4 \rho_{13} + \varepsilon^5 \rho_{14} + \cdots,
\end{aligned}$$

analogous to (2.1*a–e*), the scaled triple-deck variables t_c, x_c, $y_1 = \varepsilon^{-1} y_2$, z_c being the arguments of the desired functions. We skip a detailed analysis of the outer-flow solution, restricting ourselves to final results available in the papers cited. In the leading-order approximation, the excess pressure

$$p_{21} = p_{21}(t_c, x_c, z_c) = -\frac{1}{2\pi}\left(1 - M_\infty^2\right)^{-1/2} \times \int_{-\infty}^{\infty} \mathrm{d}\xi \int_{-\infty}^{\infty} \frac{\partial^2 A_1(t_c, \xi, \varsigma)/\partial \xi^2}{\left[\left(1 - M_\infty^2\right)^{-1}(x_c - \xi)^2 + (z_c - \varsigma)^2\right]^{1/2}} \mathrm{d}\varsigma \tag{2.9}$$

does not depend on y_2 in accord with (2.6*d*). Designating $M_0^2 = M_\infty^2 R_0(y_2) U_0^2(y_2)$, we have next

$$\begin{aligned}
p_{22} &= p_{22}(t_c, x_c, y_c, z_c)\\
&= p_{22}(t_c, x_c, 0, z_c) + \left[y_2 - \int_0^{y_2} \frac{M_\infty^2 - M_0^2(Y_2)}{M_\infty^2} \mathrm{d}Y_2\right] \frac{\partial^2 A_1}{\partial x_c^2}.
\end{aligned} \tag{2.10}$$

The third-order term $\bar{p}_{23}^{(\kappa)}$ does not enter the analysis below, and the fourth-order term

$$p_{24}^{(\kappa)} = p_{24}^{(\kappa)}(t_c, x_c, y_2, z_c) \tag{2.11}$$

as specified by (2.7). An arbitrary function

$$p_{24}^{(\kappa)}(t_c, x_c, 0, z_c) = \overline{\kappa} A_1(t_c, x_c, z_c)$$

derives from the fourth-order matching of (2.8) with the outer-flow solution, whence

$$p_{24}^{(\kappa)} = \overline{\kappa}\left[1 - R_0(y_2) U_0^2(y_2)\right] A_1(t_c, x_c, z_c). \tag{2.12}$$

The streamwise and normal-to-wall components of velocity, $\overline{u}$ and $\overline{v}$, as well as the density distribution, $\overline{\rho}$, are not required to be evaluated across the main deck to the same degree of accuracy. They may be taken in the form (2.6*a*), (2.6*b*) and (2.6*e*), respectively, because the higher-order terms in their expansions do not affect the curvature-induced contribution (2.11) to the pressure. The lateral component of velocity, $\overline{w}$, contains, in view of (2.6*c*), an additional term associated with the surface curvature. More specifically, we have

$$R_0(y_2) U_0(y_2) \frac{\partial \overline{w}}{\partial x_c} = -\varepsilon^2 \frac{\partial p_{21}}{\partial z_c} \cdots - \varepsilon^5 \overline{\kappa}\left[1 - R_0(y_2) U_0^2(y_2)\right] \frac{\partial A_1}{\partial z_c} + \cdots \tag{2.13}$$

on account of (2.12). That means the emergence of weak curvature-produced motion in the boundary layer in the direction orthogonal to the oncoming stream.

Now an expression for the excess pressure to balance centrifugal forces of different origin can be easily written down. To this end, let $y_2 \to \infty$ in (2.10), leading to an arbitrary function

$$p_{22}(t_c, x_c, 0, z_c) = p_{12}(t_c, x_c, 0, z_c) + \frac{\partial^2 A_1}{\partial x_c^2} \int_0^{\infty} \frac{M_\infty^2 - M_0^2(y_2)}{M_\infty^2} \mathrm{d}y_2.$$

https://doi.org/10.1017/S0022112005007275 Published online by Cambridge University Press

By adding two higher-order contributions to the leading-order term p_{21} in (2.9) we come to

$$\overline{p}\,(t_c, x_c, 0, z_c) = \varepsilon^2 p_{21}\,(t_c, x_c, z_c) + \varepsilon^3 D_{(xx)} \frac{\partial^2 A_1}{\partial x_c^2} + \cdots + \varepsilon^5 \overline{\kappa} A_1\,(t_c, x_c, z_c) + \cdots \quad (2.14)$$

where the integral

$$D_{(xx)} = \int_0^\infty \frac{M_\infty^2 - M_0^2\,(y_2)}{M_\infty^2}\,\mathrm{d}y_2 \quad (2.15)$$

varies with the heat-conduction regime across the body surface. The physical meaning of the curvature-related terms here are simple. Since A_1 represents the instantaneous displacement thickness, the second derivative $\partial^2 A_1/\partial x_c^2$ gives the inherent curvature of bending streamlines in the main deck with sufficient accuracy. The product $\overline{\kappa} A_1$ arises from the prescribed curvature of a solid surface. Thus, the curvature effects are different depending on whether the normal-to-wall pressure gradient stems from dynamically shaping streamlines so as to balance naturally produced centrifugal forces or the same pressure gradient has to strike a balance with centrifugal forces fixed by surface geometry. The aforementioned idea by Görtler (1955) about the equivalence of vortical flows with concave streamlines should be refined depending on environmental conditions.

3. Composite asymptotic model

It is easily seen that no curvature effects need to be accounted for to within the accuracy adopted when deriving the Prandtl equations controlling the velocity field in the thin viscous near-wall sublayer 3 where $y_{c3} = \varepsilon y_2$. The error introduced by omitting the curvature-related terms in the original Navier–Stokes equations falls beyond the scope of the asymptotic approach under examination. For example, applying the normal-to-wall distance y_{c3} to recast the $\overline{y}$-momentum conservation law in the form (2.3) we are led to an estimate

$$\frac{\partial \overline{p}}{\partial y_{c3}} = -\varepsilon^7 \overline{\kappa} R_0\,(0)\, u_{31}^2(t_c, x_c, y_{c3}, z_c),$$

$u_{31}(t_c, x_c, y_{c3}, z_c)$ being the leading-order term in an expansion

$$\overline{u} = \varepsilon u_{31} + \varepsilon^2 u_{32} + \cdots \quad (3.1)$$

for the streamwise velocity component. Analogous results follow from the continuity and the other two Navier–Stokes equations.

Let us exploit the standard affine transformation of the triple-deck theory. Then

$$t_c = C^{1/4} \tau_w^{-3/2} \left(1 - M_\infty^2\right)^{-1/4} \left(\frac{T_w^*}{T_\infty^*}\right) t, \quad (3.2a)$$

$$x_c = C^{3/8} \tau_w^{-5/4} \left(1 - M_\infty^2\right)^{-3/8} \left(\frac{T_w^*}{T_\infty^*}\right)^{3/2} x, \quad (3.2b)$$

$$y_{c3} = C^{5/8} \tau_w^{-3/4} \left(1 - M_\infty^2\right)^{-1/8} \left(\frac{T_w^*}{T_\infty^*}\right)^{3/2} y, \quad (3.2c)$$

$$z_c = C^{3/8} \tau_w^{-5/4} \left(1 - M_\infty^2\right)^{-3/8} \left(\frac{T_w^*}{T_\infty^*}\right)^{3/2} z \quad (3.2d)$$

https://doi.org/10.1017/S0022112005007275 Published online by Cambridge University Press

apply to normalize the time and spatial coordinates (Stewartson 1974; Smith 1982), the wall shear stress τ_w, being defined by (1.3) through the Chapman constant C and the ratio of the wall temperature T_w^* to the ambient temperature T_∞^*. To comply with (3.1), the corresponding components of velocity are introduced by means of

$$\overline{u} = \varepsilon C^{1/8}\tau_w^{1/4}\left(1-M_\infty^2\right)^{-1/8}\left(\frac{T_w^*}{T_\infty^*}\right)^{1/2}(u_{31}+\cdots), \tag{3.3a}$$

$$\overline{v} = \varepsilon^3 C^{3/8}\tau_w^{3/4}\left(1-M_\infty^2\right)^{1/8}\left(\frac{T_w^*}{T_\infty^*}\right)^{1/2}(v_{31}+\cdots), \tag{3.3b}$$

$$\overline{w} = \varepsilon C^{1/8}\tau_w^{1/4}\left(1-M_\infty^2\right)^{-1/8}\left(\frac{T_w^*}{T_\infty^*}\right)^{1/2}(w_{31}+\cdots), \tag{3.3c}$$

whereas the excess pressure expands as

$$\overline{p} = \varepsilon^2 C^{1/4}\tau_w^{1/2}\left(1-M_\infty^2\right)^{-1/4}(p_{31}+\cdots) \tag{3.4}$$

in accord with both $O(\varepsilon^2)$-scalings adopted for the upper and main decks. The density can be taken simply as $\overline{\rho}=R_0(0)$ in the first approximation. As a consequence, the system of Prandtl equations

$$\frac{\partial u}{\partial x}+\frac{\partial v}{\partial y}+\frac{\partial w}{\partial z}=0, \tag{3.5a}$$

$$\frac{\partial u}{\partial t}+u\frac{\partial u}{\partial x}+v\frac{\partial u}{\partial y}+w\frac{\partial u}{\partial z}=-\frac{\partial p}{\partial x}+\frac{\partial^2 u}{\partial y^2}, \tag{3.5b}$$

$$\frac{\partial w}{\partial t}+u\frac{\partial w}{\partial x}+v\frac{\partial w}{\partial y}+w\frac{\partial w}{\partial z}=-\frac{\partial p}{\partial z}+\frac{\partial^2 w}{\partial y^2} \tag{3.5c}$$

for an unsteady incompressible boundary layer comes into operation. The velocity field varying in three directions derives from swirling waves incorporating the Görtler vortical eigenmodes. To simplify notation, the subscript 3 is omitted from labelling the normal-to-wall distance and desired functions.

The matching of self-induced pressures in an intermediate domain where the main and lower decks overlap provides the interaction law

$$p=-\frac{1}{2\pi}\int_{-\infty}^{\infty}\mathrm{d}\xi\int_{-\infty}^{\infty}\frac{\partial^2 A/\partial\xi^2}{\left[\left(1-M_\infty^2\right)^{-1}(x-\xi)^2+(z-\varsigma)^2\right]^{1/2}}\,\mathrm{d}\varsigma+\varepsilon D_0\frac{\partial^2 A}{\partial x^2}+\varepsilon^3\overline{\kappa}DA \tag{3.6}$$

with the instantaneous displacement thickness $-A_1$ transformed through

$$A_1 = C^{5/8}\tau_w^{-3/4}\left(1-M_\infty^2\right)^{-1/8}\left(\frac{T_w^*}{T_\infty^*}\right)^{3/2}A. \tag{3.7}$$

Two similarity parameters

$$D_0 = D_{(xx)}C^{-3/8}\tau_w^{5/4}\left(1-M_\infty^2\right)^{7/8}\left(\frac{T_w^*}{T_\infty^*}\right)^{-3/2}, \tag{3.8a}$$

$$D = C^{3/8}\tau_w^{-5/4}\left(1-M_\infty^2\right)^{1/8}\left(\frac{T_w^*}{T_\infty^*}\right)^{3/2}, \tag{3.8b}$$

depend on the nature of centrifugal forces created either by the curvature $\partial^2 A/\partial x^2$ of dynamically shaping streamlines or by the fixed curvature $\overline{\kappa}$ of a solid surface.

https://doi.org/10.1017/S0022112005007275 Published online by Cambridge University Press

The $O(\varepsilon)$-term involving the second derivative $\partial^2 A/\partial x^2$ suggests that the shorter the distance within which naturally bending streamlines deviate from their initial location is, the more significant the contribution of centrifugal forces to a balance with the self-induced pressure becomes. On the contrary, with growing deviation distance the magnitude of this contribution sharply decreases. The $O(\varepsilon^3)$-term which stems from the fixed curvature $\bar{\kappa}$ of the solid surface does not vary with the scaled distance at all. Clearly, the curvature effects under discussion induce two separate side bands of wavelengths with the Tollmien–Schlichting oscillation spectrum in between.

Limit and boundary conditions are required at this stage to make the formulation of the problem complete. The limit conditions at the upper part $y \to \infty$ of the near-wall sublayer are obtainable from matching with a solution for most of the boundary layer. Calculating values of the first-order functions in (2.6*a–e*) we have the limit conditions

$$u - y = A(t, x, z) + O(y^{-1}), \tag{3.9a}$$

$$w = O(y^{-1}) \tag{3.9b}$$

as $y \to \infty$, to be imposed on the streamwise and lateral components of the velocity vector. This crude approximation is sufficient for our purposes. If necessary, the $O(y^{-1})$-term in (3.9*a*) can be cast in an explicit form by using the second-order solution for the main deck available in Stewartson (1974) and Ryzhov (1980). An analogous $O(y^{-1})$-term in (3.9*b*) comes directly from (2.6*c*), whereas (2.13) applies to provide the curvature-related correction. The no-slip conditions are

$$u = v = w = 0 \qquad at \quad y = 0 \tag{3.10}$$

if neither local humps nor dents are present on a smooth surface.

The two spectral side bands need to be examined closely. The term with $\partial^2 A/\partial x^2$ on the right-hand side of (3.6) attains the same order in magnitude as the integral term when the triple-deck distance x shrinks to $x = O(\varepsilon)$. Otherwise the second-order term remains much smaller than the leading-order one. However oscillations having a typical wavelength $\lambda_x = O(\varepsilon)$ damp out in time and space since they fall into a parameter domain located far beyond the upper branch of the neutral stability curve. A typical wavelength of the upper branch eigenmodes is estimated as $\lambda_x = O(Re^{-9/20})$ or $\lambda_x = O(\varepsilon^{18/5})$ in terms of ε (Bodonyi & Smith 1981). Accordingly, the side band which is associated with the curvature effects created by dynamically shaping streamlines appears to be absorbed into the upper-branch spectrum of eigen-frequencies and wavenumbers. Therefore, the second-order term on the right-hand side of (3.6) is discarded to reduce the interaction law to

$$p = -\frac{1}{2\pi}\int_{-\infty}^{\infty} \mathrm{d}\xi \int_{-\infty}^{\infty} \frac{\partial^2 A/\partial \xi^2}{\left[\left(1 - M_\infty^2\right)^{-1}(x-\xi)^2 + (z-\varsigma)^2\right]^{1/2}}\,\mathrm{d}\varsigma + \varepsilon^3 \bar{\kappa} D A. \tag{3.11}$$

The spectral content of the other side band related to the spiral-type Görtler vortices comes from a more delicate analysis, given below.

Criss-cross interaction

The Görtler vortical periodic structures are known to be tightly packed and elongated in the streamwise direction (Saric 1994). Let us exploit this observation in an attempt to further simplify the interaction law. To be specific we assume that

$$x = \frac{x_G}{\delta_x}, \tag{3.12a}$$

$$z = \delta_z z_G \tag{3.12b}$$

https://doi.org/10.1017/S0022112005007275 Published online by Cambridge University Press

where $\delta_x/\varepsilon \to 0$, $\delta_z/\varepsilon \to \infty$ as $\varepsilon \to 0$ and x_G, z_G are both $O(1)$. This two-parameter scaling agrees with that introduced by Rozhko & Ruban (1987) and shown by Timoshin (1990) and Denier *et al.* (1991) to be characteristic of the triple-deck-type asymptotic regime. The starting point is to evaluate the z-derivative

$$\frac{\partial I}{\partial z} = -\frac{1}{2\pi}\frac{\partial^2}{\partial x^2}\int_{-\infty}^{\infty}(\varsigma - z)\,\mathrm{d}\varsigma \int_{-\infty}^{\infty}\frac{A(t,\xi,\varsigma)}{\left[\left(1-M_\infty^2\right)^{-1}(x-\xi)^2+(z-\varsigma)^2\right]^{3/2}}\,\mathrm{d}\xi \tag{3.13}$$

of the integral term $I(x, z)$ on the right-hand side of (3.11). A change to new variables

$$\frac{x_G}{\delta_x} - \xi = \xi', \qquad \delta_z z_G - \varsigma = \varsigma'$$

proves to be crucial for deriving a simplified version of (3.13). If $\xi' = O(1)$ then the integrand

$$\frac{A(t, x_G/\delta_x - \xi', \delta_z z_G - \varsigma')}{\left[\left(1-M_\infty^2\right)^{-1}\xi'^2 + \varsigma'^2\right]^{3/2}} \to \frac{A(t, x_G/\delta_x, \delta_z z_G - \varsigma')}{\left[\left(1-M_\infty^2\right)^{-1}\xi'^2 + \varsigma'^2\right]^{3/2}}, \tag{3.14}$$

whereas for $x_G/\delta_x - \xi' = O(1)$ and $\xi' = O(x_G/\delta_x) \to \infty$ we have

$$\frac{A(t, x_G/\delta_x - \xi', \delta_z z_G - \varsigma')}{\left[\left(1-M_\infty^2\right)^{-1}\xi'^2 + \varsigma'^2\right]^{3/2}} \to 0. \tag{3.15}$$

Hence (3.13) reduces to approximately

$$\frac{\partial I}{\partial z} = \frac{1}{\pi}\left(1-M_\infty^2\right)^{\frac{1}{2}}\int_{-\infty}^{\infty}\frac{\partial^2 A(t,x,\varsigma)/\partial x^2}{z-\varsigma}\,\mathrm{d}\varsigma \tag{3.16}$$

with a consequence that the interaction law becomes

$$\frac{\partial p}{\partial z} = \frac{1}{\pi}\left(1-M_\infty^2\right)^{\frac{1}{2}}\int_{-\infty}^{\infty}\frac{\partial^2 A(t,x,\varsigma)/\partial x^2}{z-\varsigma}\mathrm{d}\varsigma + \varepsilon^3\overline{\kappa}D\frac{\partial A}{\partial z} \tag{3.17}$$

where the similarity parameter D obeys (3.8*b*).

It follows from (3.14) and (3.15) that the physical meaning of replacing the double integral (3.13) with the single integral (3.16) is that the contribution from the Görtler vortical range of reference lengths prevails over the contribution coming from the Tollmien–Schlichting wave scales in the viscous/inviscid interaction regime under consideration. As has been mentioned, this regime differs from the wave/vortex interactions in Hall & Smith (1988, 1989, 1991) where the surface curvature $\overline{\kappa}$ can play no role at all. The change in the interaction law will be shown below to lead to far-reaching conclusions. The Cauchy problem for the system of linearized Prandtl equations (3.5*a–c*) supplemented with the interaction law (3.17) proves to be ill-posed. Evidently, this is an outcome of ignoring the pressure variations induced through viscous/inviscid interaction in the Tollmien–Schlichting spectral range that embraces all characteristic wavelengths intrinsic to the swirling waves on curved surfaces. For steady incompressible boundary layers, a simplified version of the interaction law, analogous to (3.17), has been introduced by Rozhko & Ruban (1987). Ruban (1990*a*, *b*) commented on the ill-posedness of the Cauchy problem formulated within the framework of this mathematical model. Specifically, the model applies to disturbance patterns confined to the Görtler vortical side band of eigen-frequencies and wavelengths. The ill-posedness of the Cauchy problem originates from an unrealistic growth of the amplitude amplification rate with large streamwise

https://doi.org/10.1017/S0022112005007275 Published online by Cambridge University Press

wavenumbers in the Tollmien–Schlichting spectral range (see below). On the strength of (3.12a,b), an estimate

$$\delta_x^2 \delta_z = O(\varepsilon^3) \tag{3.18}$$

determines the scaling of unsteady vortical structures. One more scaling condition to be imposed on spatial variables is necessary to fix δ_x and δ_z.

4. Spectra of free oscillations

Since the Prandtl equations are nonlinear, they allow us in principle to study wave motion of finite amplitude. However, usually the boundary-layer receptivity to external excitation and an earlier stage of disturbance development mean a linear process which is brought about by a weak perturbing source. Setting

$$(u - y, v, w, p, A) = a(\widetilde{u}, \widetilde{v}, \widetilde{w}, \widetilde{p}, \widetilde{A}), \qquad a \to 0, \tag{4.1}$$

let us simplify the Prandtl equations (3.5a–c) as well as the limit conditions (3.9a,b) and no-slip conditions (3.10). To cover the whole spectrum of swirling waves on a concave surface, the interaction law is taken in the form (3.11) rather than its simplified version (3.17).

Dispersion relation

A class of travelling-wave-type solutions is defined as

$$(\widetilde{u}, \widetilde{v}, \widetilde{w}, \widetilde{p}, \widetilde{A}) = \mathrm{e}^{\omega t + \mathrm{i}(kx+mz)} [\overline{u}_c(y), \overline{v}_c(y), \overline{w}_c(y), \overline{p}_c, \overline{A}_c]. \tag{4.2}$$

Substitution of (4.1) and (4.2) into the system of linearized Prandtl equations results in a set of homogeneous ordinary differential equations

$$\frac{\mathrm{d}\overline{v}_c}{\mathrm{d}y} = -\mathrm{i}\,(k\overline{u}_c + m\overline{w}_c)\,, \tag{4.3a}$$

$$\frac{\mathrm{d}^2\overline{u}_c}{\mathrm{d}y^2} = (\omega + \mathrm{i}ky)\,\overline{u}_c + \overline{v}_c + \mathrm{i}k\overline{p}_c, \tag{4.3b}$$

$$\frac{\mathrm{d}^2\overline{w}_c}{\mathrm{d}y^2} = (\omega + \mathrm{i}ky)\,\overline{w}_c + \mathrm{i}m\overline{p}_c \tag{4.3c}$$

for the complex-valued functions $\overline{u}_c$, $\overline{v}_c$, $\overline{w}_c$. The limit conditions (3.9a,b) at infinity lead to

$$\overline{u}_c \to \overline{A}_c, \tag{4.4a}$$

$$\overline{w}_c \to 0, \tag{4.4b}$$

as $y \to \infty$. The first linear algebraic equation

$$\overline{p}_c = \left\{k^2\left[k^2 + \left(1 - M_\infty^2\right)^{-1} m^2\right]^{-1/2} + \varepsilon^3 \overline{\kappa} D\right\} \overline{A}_c \tag{4.5}$$

to connect p_c entering (4.3b,c) and $\overline{A}_c$ from the right-hand side of (4.4a) comes from the interaction law (3.11) with D given in (3.8b). The no-slip conditions (3.10) become

$$\overline{u}_c = \overline{v}_c = \overline{w}_c = 0 \qquad \text{at} \quad y = 0. \tag{4.6}$$

Thus we are led to an eigenvalue problem that specifies the frequency and wavenumber spectra of free oscillations.

The standard technique (see for example Ryzhov & Terent'ev 1986, 1998) which relies on introducing a new independent variable

$$Y = \Omega + \mathrm{i}^{1/3} k^{1/3} y, \tag{4.7a}$$

$$\Omega = \mathrm{i}^{-2/3} \omega k^{-2/3} \tag{4.7b}$$

https://doi.org/10.1017/S0022112005007275 Published online by Cambridge University Press

and a new desired function $F = k\overline{u}_c + m\overline{v}_c$, serves to solve the eigenvalue problem under consideration. It should be mentioned that a cut along the positive imaginary semi-axis is drawn in the complex k-plane which isolates a single-valued branch of the function $k^{1/3}$ by means of $-\frac{3}{2}\pi < \arg(k) < \frac{1}{2}\pi$ with a consequence that $-\frac{1}{3}\pi < \arg(Y) < \frac{1}{3}\pi$ as $y \to \infty$.

It is easily seen that F satisfies precisely the same equation that controls the propagation of the normal Tollmien–Schlichting waves in a Blasius boundary layer. This property is the essence of a transformation by Squire (1933) which remains valid asymptotically, as $\varepsilon \to 0$, even for swirling waves with an inherent component of Görtler vortices caused by centrifugal forces. Applying the limit condition for F as $|Y| \to \infty$ that follows from (4.4*a*, *b*) yields the second linear algebraic equation

$$\overline{p}_c = \mathrm{i}^{-1/3} k^{5/3} (k^2 + m^2)^{-1} \Phi(\Omega) \overline{A}_c \tag{4.8}$$

that connects $\overline{p}_c$ and $\overline{A}_c$. Here the Airy function $\mathrm{Ai}(\Omega)$ is used to define a function

$$\Phi = \frac{\mathrm{dAi}\,(\Omega)}{\mathrm{d}Y}\,[I\,(\Omega)]^{-1}, \tag{4.9a}$$

$$I = \int_{\Omega}^{\infty} \mathrm{Ai}\,(Y)\,\mathrm{d}Y \tag{4.9b}$$

widely in use in the triple-deck theory. Eliminating the ratio $\overline{p}_c/\overline{A}_c$ between (4.5) and (4.8) we arrive at the dispersion relation

$$\Phi\,(\Omega) = Q(k, m; M_\infty, \varepsilon, \overline{\kappa} D). \tag{4.10}$$

The right-hand side

$$Q = \mathrm{i}^{1/3} \frac{k^2 + m^2}{k^{5/3}} \left\{ \frac{k^2}{\left[k^2 + \left(1 - M_\infty^2\right)^{-1} m^2\right]^{1/2}} + \varepsilon^3 \overline{\kappa} D \right\} \tag{4.11}$$

depends on both wavenumbers k and m, the Mach number M_∞, the Reynolds number $Re = \varepsilon^{-1/8}$ and the surface curvature $\overline{\kappa}$ multiplied by D.

The product $\varepsilon^3 \overline{\kappa} D$ is a characteristic feature of the composite asymptotic model embracing both the Tollmien–Schlichting waves and spiral-type Görtler vortices. However, the key property of Q cast in the form (Ryzhov & Terent'ev 1986, 1998)

$$\arg\,[Q\,(k, m; M_\infty, \varepsilon, \overline{\kappa} D)] = \begin{cases} \frac{1}{6}\pi & \text{if} \quad \arg\,(k) = 0, \\ -\frac{1}{6}\pi & \text{if} \quad \arg\,(k) = -\pi \end{cases} \tag{4.12}$$

remains valid no matter what the sign of the real lateral wavenumber m is and which values ε and $M_\infty < 1$ take. A constraint $\overline{\kappa} > 0$ specifying a concave surface prevents the expression in the braces from passing through zero and taking on negative values. Experimentally, unstable Görtler vortices are observed on concave surfaces; a short discussion of their evolution over convex walls is available in Floryan (1991). Within the framework of the asymptotic analysis, the amplitude attenuation rate $Re\,[\omega_{1,vort}(k)] < 0$ for vortical part of disturbances on a convex surface with $\overline{\kappa} < 0$.

Side band

In compliance with (3.12*a*, *b*), $k \to 0$ and $m \to \infty$ in the spectral range of spiral-type Görtler vortices. In view of (4.11), it follows that $k^{1/3} m = O(1)$ or $\delta_x^{1/3}/\delta_z = O(1)$ as $\varepsilon \to 0$. Combined with (3.18) the last order-of-magnitude estimate leads to the rescaling

https://doi.org/10.1017/S0022112005007275 Published online by Cambridge University Press

$\delta_x = O(\varepsilon^{9/7})$, $\delta_z = O(\varepsilon^{3/7})$ of the streamwise and lateral dimensions of unsteady vortical structures. As it was claimed aboved, the ratio $\delta_x^2/\varepsilon^2 = O(\varepsilon^{4/7})$ tends to zero with $\varepsilon \to 0$. From (4.7*b*), the corresponding estimate for ω becomes $O(\varepsilon^{6/7})$. Thus the spiral Görtler vortices on a concave surface are born in the spectral side band

$$\omega = \varepsilon^{6/7}\,\omega_G = Re^{-3/28}\,\omega_G \approx 0.25\,\omega_G, \tag{4.13a}$$

$$k = \varepsilon^{9/7}\,k_G = Re^{-9/56}\,k_G \approx 0.12\,k_G, \tag{4.13b}$$

$$m = \varepsilon^{-3/7}\,m_G = Re^{3/56}\,m_G \approx 2.02\,m_G \tag{4.13c}$$

of eigen-frequencies and wavenumbers labelled G, where the correction term in the braces on the right-hand side of (4.11) attains the same order in magnitude as the leading-order term for typical transition conditions with $Re \approx 5 \times 10^5$. Transformed to new spectral parameters, the expression for Q becomes

$$Q = \mathrm{i}^{1/3}\frac{Re^{-3/7}k_G^2 + m_G^2}{k_G^{5/3}}\left\{\frac{k_G^2}{\left[Re^{-3/7}k_G^2 + \left(1 - M_\infty^2\right)^{-1} m_G^2\right]^{1/2}} + \overline{\kappa}D\right\}. \tag{4.14}$$

Here both terms play an equal role in determining the boundary layer stability. By virtue of (4.7*b*), the auxiliary combination Ω remains invariant under the affine transformation (4.13*a*, *b*), i.e.

$$\Omega = \Omega_G = \mathrm{i}^{-2/3}\omega_G k_G^{-2/3}.$$

Both $O(Re^{-3/7})$-terms need to be kept in (4.14) to render the Cauchy problem well-posed in a linear approximation. For incompressible flows, an analogous dispersion relation was proposed in an upublished paper by Ruban, Türkyilmazoglu & Gajjar (1998) to remove the ill-posedness of the Cauchy problem from the criss-cross interaction scheme. Based on this approach, the authors came to the conclusion that no upstream influence occurred at large times when the wave packets became fully developed and were swept downstream.

Rescaling of the eigen-frequencies and wavenumbers fixed by (4.13*a–c*) implies a change to new independent variables

$$t = \varepsilon^{-6/7}t_G = Re^{3/28}t_G, \tag{4.15a}$$

$$x = \varepsilon^{-9/7}x_G = Re^{9/56}x_G, \tag{4.15b}$$

$$z = \varepsilon^{3/7}z_G = Re^{-3/56}z_G \tag{4.15c}$$

in place of the canonical triple-deck time (3.2*a*) and space coordinates (3.2*b*, *d*) within the spectral side band typical of spiral-type vortices. Hence it follows that with the Reynolds number $\mathrm{Re} \approx 5 \times 10^5$ characteristic of transition environments the streamwise dimensions of the Görtler vortex is about ten times as large as the characteristic length of a Tollmien–Schlichting wave. On the other hand, the Görtler vortices are closely spaced and the lateral extent of a single vortex is only one half the width of a three-dimensional Tollmien–Schlichting wave. In line with experimental evidence Saric (1994), the spiral-type vortices form elongated tightly packed structures on a concave surface. Rescaling of the triple-deck normal-to-wall distance (3.2*c*) in line with (4.15*a–c*) gives

$$y = \varepsilon^{-3/7}y_G = Re^{3/56}y_G \approx 2.0y_G. \tag{4.16}$$

https://doi.org/10.1017/S0022112005007275 Published online by Cambridge University Press

The velocity field

$$u = \varepsilon^{-3/7} u_G = Re^{3/56} u_G,$$
$$v = \varepsilon^{3/7} v_G = Re^{-3/56} v_G,$$
$$w = \varepsilon^{9/7} w_G = Re^{-9/56} w_G$$

created by the spiral-type vortical disturbances can be easily found by using the governing equations (3.5*a–c*). An assessment of the magnitude of the self-induced pressure requires some care. From the z-momentum equation we deduce that

$$p = 0(w^2) = \varepsilon^{18/7} p_G = Re^{-9/28} p_G. \tag{4.17}$$

Then the continuity equation (3.5*a*) and the z-momentum equation (3.5*c*) remain intact under the transformation to new variables. However, the x-momentum equation (3.5*b*) becomes

$$\frac{\partial u_G}{\partial t_G} + u_G \frac{\partial u_G}{\partial x_G} + v_G \frac{\partial u_G}{\partial y_G} + w_G \frac{\partial u_G}{\partial z_G} = -Re^{-3/7} \frac{\partial p_G}{\partial x_G} + \frac{\partial^2 u_G}{\partial y_G^2}$$

where an $O(Re^{-3/7})$ term arises from the streamwise pressure gradient and drops out in the theory of criss-cross interaction (Rozhko & Ruban 1987; Ruban 1990*a*, *b*). A change to the new variables shows that no curvature effects appear in the Prandtl equations controlling the fluid motion in the thin viscous near-wall sublayer. The curvature effects prove to be negligible in the limit of reference times and wavelengths determining the evolution of vortical structures. This limiting case lends credence to the composite model where the curvature-related term $\varepsilon^3 \overline{\kappa} DA$ is included in the interaction law (3.11) but no additional terms are present in the Prandtl equations. Also, the streamwise pressure gradient becomes $O(Re^{-3/7})$ small when passing to the limit of spiral Görtler vortices in the x-momentum equation. In view of (4.17), the self-induced pressure drops to $O(Re^{-9/28}) \approx 0.015$ of its original magnitude in the Tollmien–Schlichting spectral range. The Tollmien–Schlichting waves appear as large-amplitude short-scaled disturbances propagating against the background of much weaker long-scaled vortical structures.

5. Dispersion curves

Before we proceed to elucidate the behaviour of the dispersion curves controlling the stability properties of the wave/vortex disturbance patterns, let us perform one more affine transformation

$$\omega_G \to (\overline{\kappa} D)^{2/7} \omega_G, \tag{5.1a}$$
$$k_G \to (\overline{\kappa} D)^{3/7} k_G, \tag{5.1b}$$
$$m_G \to (\overline{\kappa} D)^{-1/7} m_G. \tag{5.1c}$$

The auxiliary variable Ω_G remains invariant whereas the right-hand side Q of the dispersion relation reduces to the form

$$Q = \mathrm{i}^{1/3} \frac{D_G k_G^2 + m_G^2}{k_G^{5/3}} \left\{ \frac{k_G^2}{\left[D_G k_G^2 + \left(1 - M_\infty^2\right)^{-1} m_G^2 \right]^{1/2}} + 1 \right\} \tag{5.2}$$

https://doi.org/10.1017/S0022112005007275 Published online by Cambridge University Press

where the Reynolds number Re and the product $\bar{\kappa}D$ are combined in a similarity parameter

$$D_G = Re^{-3/7}(\bar{\kappa}D)^{8/7} = D^{8/7}\left(\frac{Re}{\bar{\kappa}^{8/3}}\right)^{-3/7}. \tag{5.3}$$

It is worth noting that this parameter incorporating Re and $\bar{\kappa}$ is in marked contrast to the Görtler number defined in (1.2).

Complex Ω_G-plane

We are now in a position to describe new properties of conceptual significance that arise from coupling the two eigenmodes of different physical nature. Some preliminary results have been reported in Ryzhov (2003) and Ryzhov & Bogdanova-Ryzhova (2003). An analysis of the dispersion curves in the auxiliary Ω_G-plane is pertinent first, because it allows us to predict the existence of a new eigenmode capable of driving disturbances upstream, against the direction of an oncoming boundary layer. We begin by noting that $Q(k) = \mathrm{i}^{1/3}k^{1/3}|k|$ is the right-hand side of the dispersion relation (4.10) for normal Tollmien–Schlichting waves in the Blasius boundary layer (Ryzhov & Terent'ev 1986, 1998). Evidently $\arg[Q(k_G, m_G; M_\infty, D_G)]$ equals $\arg[Q(k, m; M_\infty, \varepsilon, \bar{\kappa}D)]$ determined by (4.12) for both $\arg(k_G) = \arg(k) = 0$ and $\arg(k_G) = \arg(k) = -\pi$. Hence $\arg[Q(k_G, m_G; M_\infty, D_G)]$ coincides with the argument of $Q(k)$ no matter what the sign of the lateral wavenumber m_G is and which values $M_\infty < 1$ and D_G take. This provides a clue to understanding how the dispersion-relation properties of these two-dimensional disturbances can be exploited to study the more general case of interest. In what follows, $m_G = m_{G0}$ is kept fixed.

With some specific value of k_G, the dispersion-relation roots form, as in the two-dimensional case, a countable set of image points in the Ω_G-plane. When k_G varies taking real values, these points move along trajectories which constitute a collection of dispersion curves. Figure 1 shows a typical map of the dispersion relation (4.10) with right-hand side (4.11) or, alternatively, (5.2) onto the complex Ω_G-plane obtained from the corresponding plot of the trajectories for normal Tollmien–Schlichting waves in the Blasius boundary layer. However, Q in (5.2) does not vanish to zero in the limit $k_G \to 0$ unless $m_{G0} = 0$. Therefore, none of the image points approach the real negative semi-axis in figure 1. On the contrary, they remain separated by finite distances from the points Ω_{dj}, $j = 1, 2, \ldots$, the roots of the equation $\mathrm{dAi}(\Omega_{\mathrm{d}j})/\mathrm{d}Y = 0$. This distinction leads to dramatic alterations in the boundary-layer response to infinitesimal perturbations which come from the destabilizing effects of centrifugal forces supported by the surface curvature.

Our concern is primarily with the first dispersion curve $\Omega_{G1}(k_G, m_{G0}; M_\infty, D_G)$. The three parameters m_{G0}; M_∞, D_G are omitted below from the notation of the dispersion curves in all complex planes. Consider in more detail the image-point motion along $\Omega_{G1}(k_G)$ provided that k_G takes positive as well as negative real values. By virtue of (4.12), the asymptotic behaviour of $\Omega_{G1}(k_G)$ as $k_G \to -\infty$ is established by

$$\Omega_{G1} \to \infty \exp\left(\tfrac{5}{6}\pi\mathrm{i}\right) \tag{5.4}$$

analogous to the first dispersion curve for normal Tollmien–Schlichting waves in the Blasius boundary layer, no matter how small the parameter $D_G \neq 0$ is. An increase in $k_G < 0$ leads to downward motion along the upper branch of the curve to a certain limiting point $\Omega^{(-)}_{G1\,\mathrm{lim}}$ whose position varies with the magnitude of m_{G0} and also depends on M_∞ and D_G. Upon reaching the limiting point, the motion along the first dispersion curve changes to the opposite direction and the image point starts

https://doi.org/10.1017/S0022112005007275 Published online by Cambridge University Press

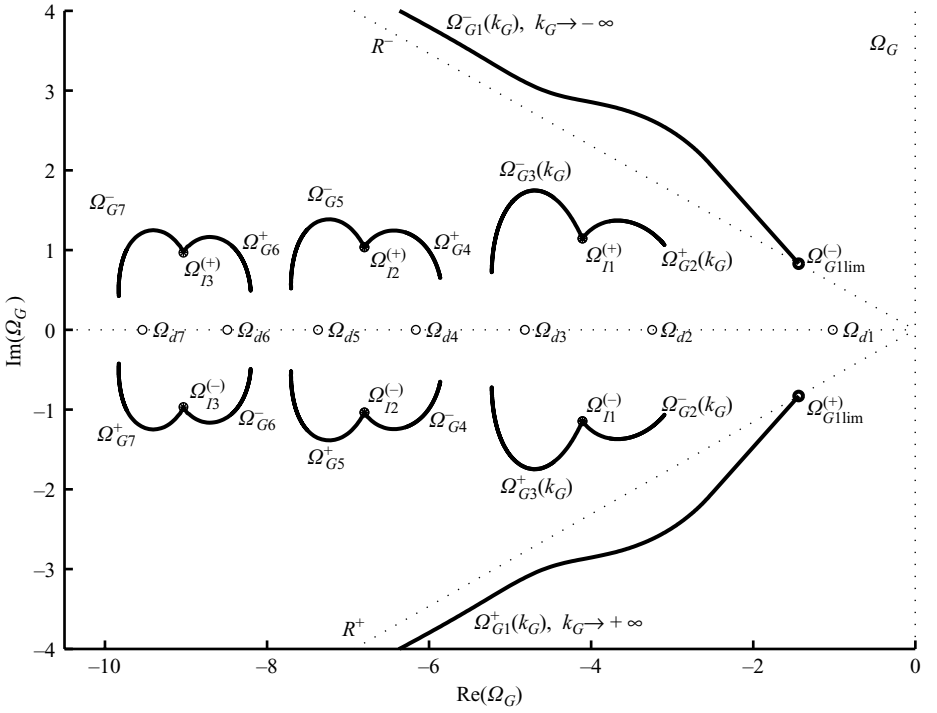


FIGURE 1. Auxiliary Ω_G-plane with end-points $\Omega^{(\pm)}_{G1\,\mathrm{lim}}$ which bring about absolute instability in the streamwise direction. The complex-valued variable $\Omega=\Omega_G$ is an invariant.

climbing upwards. As a result, (5.4) again comes into operation as $k_G\to-0$. The passage through $k_G=0$ is marked by a sudden jump of the image point onto the branch of the dispersion curve located symmetrically about the real axis in the lower half-plane of the Ω_G-plane, the corresponding asymptotics being

$$\Omega_{G1}\to\infty\exp\left(-\frac{5}{6}\pi\mathrm{i}\right) \tag{5.5}$$

as $k_G\to+0$. A further increase in $k_G>0$ results in upward motion along the lower branch of the curve to the limiting point $\Omega^{(+)}_{G1\,\mathrm{lim}}$ which is a mirror image of $\Omega^{(-)}_{G1\,\mathrm{lim}}$. Upon reaching $\Omega^{(+)}_{G1\,\mathrm{lim}}$ and making a sharp downward turn here the image point proceeds along the same branch in the opposite direction to complete its motion with the asymptote (5.5), as $k_G\to\infty$. The most important feature of this map is that the image point does not attain the first zero Ω_{d1} of the derivative of the Airy function. In consequence, the first dispersion curve divides into two branches. Both branches are covered twice by the image point in its forward and reverse motions. Only in the case of two-dimensional oscillations with $m_{G0}=0$ do the two isolated branches merge at Ω_{d1} to produce a double point. The motion of the image point from $\Omega^{(-)}_{G1\,\mathrm{lim}}$ to upward infinity and from $\Omega^{(+)}_{G1\,\mathrm{lim}}$ to downward infinity implies the formation of a new eigenmode endowed with unusual properties.

In line with conventional practice, the conclusion about the stability of the boundary layer on a concave surface rests upon the sign of $\mathrm{Re}(\omega_{G1})$ in the definition (4.2) of travelling waves. Neutral oscillations separating stable and unstable oscillations are

https://doi.org/10.1017/S0022112005007275 Published online by Cambridge University Press

prescribed by $\mathrm{Re}(\omega_{G1})=0$, whence

$$\arg(\Omega_{G*}) = \begin{cases} -\frac{5}{6}\pi, \text{ if } \arg(k_{G*}) = 0, \arg(\omega_{G*}) = -\frac{1}{2}\pi, \\ \frac{5}{6}\pi, \quad \text{if } \arg(k_{G*}) = -\pi, \arg(\omega_{G*}) = \frac{1}{2} \end{cases}$$

where an asterisk in the subscript relates to critical values of the frequency and wavenumber. Accordingly, a domain of unstable swirling waves is bounded in the complex Ω_G-plane by conditions

$$-\tfrac{5}{6}\pi < \arg(\Omega_G) < \tfrac{1}{6}\pi, \qquad \text{if} \quad \arg(k_G) = 0, \tag{5.6}$$

$$-\tfrac{1}{6}\pi < \arg(\Omega_G) < \tfrac{5}{6}\pi, \qquad \text{if} \quad \arg(k_G) = -\pi. \tag{5.7}$$

The rays R^+ and R^- shown in figure 1 by dotted lines are fixed by $\arg(\Omega_G)=-\frac{5}{6}\pi$, $\arg(k_G)=0$ and $\arg(\Omega_G)=\frac{5}{6}\pi$, $\arg(k_G)=-\pi$. Both rays can cross only the first dispersion curve $\Omega_{G1}(k_G)$. Evidently, the points of possible intersections correspond to neutral waves of the temporal stability approach. However, whether these intersections actually take place with a given set of values of m_{G0}; M_∞, D_G depends on the location of the limiting points $\Omega^{(\pm)}_{G1\,\mathrm{lim}}$ on the upper and lower branches of the first dispersion curve $\Omega_{G1}(k_G)$. If they are positioned inside a sector shaped by the rays R^+ and R^-, two different values of the neutral frequency come into play. On the other hand, when the limiting points fall outside this sector, there is no neutral frequency at all. A single value of the neutral frequency occurs with the proviso that $\Omega^{(+)}_{G1\,\mathrm{lim}}$ coincides with the point where R^+ crosses the lower branch of the first dispersion curve and $\Omega^{(-)}_{G1\,\mathrm{lim}}$ gives the point of intersection of R^- with the upper branch of the same curve. This is just the case depicted in figure 1. With the limiting point lying outside the sector between R^+ and R^-, all types of swirling waves specified by the lateral wavenumber m_{G0} and the values of similarity parameters M_∞ and D_G are unstable.

Complex ω_G-plane for small m_{G0}

Let us consider some important repercussions of the fact that each of the branches of $\Omega_{G1}(k_G)$ is covered twice by the image point in its motion on an infinite interval $-\infty < k_G < \infty$. In order to gain insight into principal features of the dispersion curves in the complex frequency plane ω_G we start from the two-term expansion

$$\Phi(\Omega_G) \sim -\Omega_G - \Omega_G^{-\frac{1}{2}} + \cdots \qquad \text{as} \quad |\Omega_G| \to \infty$$

in the auxiliary Ω_G-plane that follows from (4.9*a*) and derive an expression

$$\begin{aligned} \omega_{G1} \sim -\mathrm{i}\frac{D_G k_G^2 + m_{G0}^2}{k_G} & \left\{ \frac{k_G^2}{\left[D_G k_G^2 + \left(1 - M_\infty^2\right)^{-1} m_{G0}^2\right]^{1/2}} + 1 \right\} \\ & + \frac{\sqrt{2}}{2}\left[1 - \mathrm{isign}(k_G)\right] \frac{|k_G|^{3/2}}{\left(D_G k_G^2 + m_{G0}^2\right)^{1/2}} \\ & \times \left\{ \frac{k_G^2}{\left[D_G k_G^2 + \left(1 - M_\infty^2\right)^{-1} m_{G0}^2\right]^{1/2}} + 1 \right\}^{-\frac{1}{2}} + \cdots \end{aligned} \tag{5.8}$$

determining the asymptotic behaviour of $\omega_{G1}(k_G)$ in two limits, as $k_G \to \pm\infty$ and $k_G \to \pm 0$.

https://doi.org/10.1017/S0022112005007275 Published online by Cambridge University Press

If $k_G \to \pm\infty$, (5.8) converges to

$$\mathrm{Re}[\omega_{G1}(k_G)] \to \frac{\sqrt{2}}{2} D_G^{-1/4} \tag{5.9}$$

with the similarity parameter D_G entering the right-hand side. This limit specifies the Tollmien–Schlichting spectral range of swirling waves. Returning from ω_G and k_G to ω and k by means of (4.13*a*), (5.1*a*) and (4.13*b*), (5.1*b*), respectively, and taking into account the definition of D_G in (5.3) the limit

$$\mathrm{Re}\,[\omega_1(k)] \to \frac{\sqrt{2}}{2} \qquad \text{as } |k| \to \infty$$

is retrieved in the canonical triple-deck variables, independent of any parameter (Ryzhov & Terent'ev 1986, 1998). It is instructive to obtain the amplitude amplification rate within the framework of the simplified model controlled by the interaction law (3.17) and the dispersion relation (4.10) where the right-hand side

$$Q = \mathrm{i}^{1/3} \frac{m_{G0}^2}{k_G^{5/3}} \left[\left(1 - M_\infty^2\right)^{1/2} \frac{k_G^2}{|m_{G0}|} + 1 \right] \tag{5.10}$$

derives from (4.14) provided that D_G equals identically zero. Then we arrive at (Ruban 1990*a*, *b*)

$$\mathrm{Re}[\omega_{G1}(k_G)] \to \frac{\sqrt{2}}{2} \left(1 - M_\infty^2\right)^{-1/4} \left(\frac{|k_G|}{|m_{G0}|} \right)^{1/2} \qquad \text{as } k_G \to \pm\infty. \tag{5.11}$$

It is this unrealistically large growth rate which makes the Cauchy problem ill-posed, as it was mentioned above.

In the second limit $k_G \to \pm 0$, (5.8) yields

$$\mathrm{Re}[\omega_{G1}(k_G)] \to \frac{\sqrt{2}}{2} \frac{|k_G|^{3/2}}{|m_{G0}|} \tag{5.12}$$

showing that at the triple-deck scale the amplitude amplification rate

$$\mathrm{Re}[\omega_1(k)] \to \frac{\sqrt{2}}{2} Re^{3/16} (\bar{\kappa} D)^{-1/2} \frac{|k|^{3/2}}{|m_0|} \qquad \text{as } k \to 0$$

indefinitely increases with $Re \to \infty$. The same results hold in the context of the simplified model governed by (5.10). Note that the integral terms responsible for the pressure variations induced in both models by viscous/inviscid interaction become negligible to leading order for small k_G. The excess pressure comes solely from the surface curvature effects in the main deck.

The most important inference to be drawn from the asymptotic study is that the first dispersion curve divides in the complex ω_G-plane into two separate branches and each branch consists of two segments or lobes. From (5.9), the right-hand lobes pass, as $k_G \to \pm\infty$, a finite distance from the imaginary axis and generate in this limit the Tollmien–Schlichting eigenmode. In view of (5.12), both left-hand lobes asymptotically tend to the imaginary axis with $k_G \to 0$ thereby giving rise to a new eigenmode. The direction in which the image point moves along the left-hand lobes gives the new eigenmode an unusual property. The derivative $\mathrm{d}\,\mathrm{Im}(\omega_{G1})/\mathrm{d}k_G > 0$

https://doi.org/10.1017/S0022112005007275 Published online by Cambridge University Press

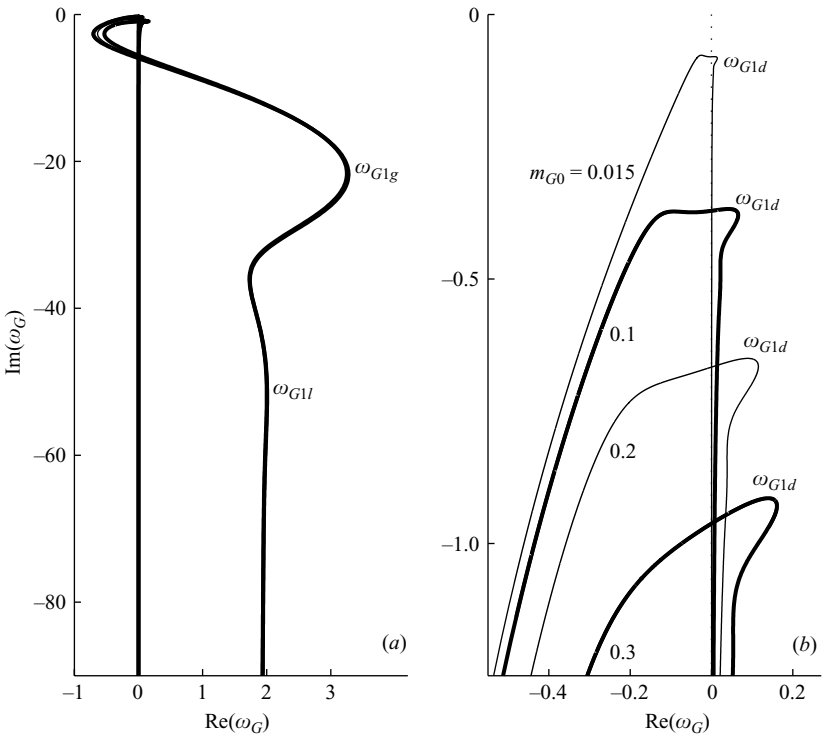


FIGURE 2. Two isolated branches of the first dispersion curve in the plane of complex frequencies for $m_{G0} \neq 0$. Each branch consists of two segments (lobes). (*b*) An enlargement of (*a*) close to the origin.

along the left-hand lobes, whereas $\mathrm{dIm}(\omega_{G1})/\mathrm{d}k_G < 0$ at each point of the right-hand lobes.

Let us assume the Mach number to be equal to zero for the time being. This assumption restricts the analysis to incompressible boundary layers but allows us to focus on the inherent characteristics of swirling waves. With the assumption that $M_\infty = 0$, the single similarity parameter D_G enters expression (5.2) for Q.

Obviously the shape of the first dispersion curve strongly depends on the lateral wavenumber m_{G0}. For all $m_{G0} \neq 0$ the first dispersion curve has two different asymptotes stretching to infinity in the lower and upper half-planes of the complex ω_G-plane. Both asymptotes are parallel to the imaginary axis and spaced $(\frac{1}{2}\sqrt{2})D_G^{-1/4}$ apart. Figure 2(*a*) presents a typical example of the first dispersion curves for $m_{G0} = 0.015, 0.1, 0.2$ and 0.3. A domain close to the origin is drawn in figure 2(*b*) on the enlarged scale for the same values of the lateral wavenumber and $\varepsilon^3\overline{\kappa}D = 0.0326$ which corresponds to $D_G = (\varepsilon^3\overline{\kappa}D)^{8/7} = 0.02$. The two symmetrically positioned branches of the first dispersion curve become separated, and in addition, neither of them meets the real axis. Each branch is made up of two segments connected with a loop into a single curve. The lower branch, starting from $\mathrm{Im}(\omega_{G1}) \to -\infty$ and $\mathrm{Re}(\omega_{G1})$ prescribed by (5.9) as $k_G \to \infty$, first climbs steeply, then turns not far from the origin and goes downwards to terminate as (5.12) with $k_G \to +0$. The upper branch, coming from $\mathrm{Im}(\omega_{G1}) \to \infty$ and the same limit (5.9) of $\mathrm{Re}(\omega_{G1})$ as $k_G \to -\infty$, is a mirror image of the lower branch, obtainable with negative values of k_G. The global and local maxima of $\mathrm{Re}(\omega_{G1})$, labelled g and l, respectively, feature the right-hand

https://doi.org/10.1017/S0022112005007275 Published online by Cambridge University Press

lobe of each branch. They induce two strong signals which merge into a single highly modulated disturbance sweeping downstream since $\mathrm{d}\,\mathrm{Im}(\omega_{G1})/\mathrm{d}k_G < 0$ at every point on the right-hand lobes. The disturbance frequencies and wavenumbers fall within the Tollmien–Schlichting spectral range.

A loop connecting both segments has a portion with a local negative minimum of $\mathrm{Re}(\omega_{G1})$ in the left half-plane of the complex ω_G-plane. Disturbances associated with this portion are stable, except for the end points, which lie on the imaginary axis and generate neutral oscillations. Thus, in line with the above analysis of the auxiliary Ω_G-plane, two different values of the neutral frequency come into play in swirling waves with small spanwise wavenumbers. One of these values does not appreciably deviate from the neutral frequency inherent in the Tollmien–Schlichting eigenmodes. The other, much lower value stems from the wave/vortex interaction capable of providing support to neutrally stable disturbances. Both values come closer as the lateral wavenumber m_{G0} increases.

Upon crossing the imaginary axis at the second neutral point, the loop enters the right half-plane $\mathrm{Re}(\omega_G) > 0$, where it gives rise to unstable vortical eigenmodes. A small positive peak d of $\mathrm{Re}(\omega_{G1})$ gradually develops in the form of the loop close to the origin. This peak triggers a relatively weak signal consisting of slightly modulated oscillation cycles. The signal advances upstream, against the direction of the oncoming boundary layer since $\mathrm{d}\,\mathrm{Im}(\omega_{G1})/\mathrm{d}k_G > 0$ along the whole length of the left-hand lobes of the first dispersion curve extending to infinity. So, the loop in the shape of either of the two branches making up the first dispersion curve in the complex frequency plane can be regarded as an outcome of the wave/vortex eigenmodes' interaction.

Variations with lateral wavenumber

Distortions in the shape of the first dispersion curve which have already surfaced in the above scrutiny of $\omega_{G1}(k_G)$ in the immediate vicinity of the origin become much larger with values of m_{G0} continuously increasing.

The plot in figure 3 computed with $m_{G0} = 0.5$ is typical of the range $0.3 < m_{G0} < 0.65$. There still exists a portion of both branches of the first dispersion curve which is situated in the left half-plane of the complex ω_G-plane with its end points on the imaginary axis. Thus, neutral oscillations persist and can have two different frequencies. However, this portion becomes shorter and has a weaker local negative minimum of $\mathrm{Re}(\omega_{G1})$ until the image point in its motion along the first dispersion curve $\Omega_{G1}(k_G)$ in the auxiliary Ω_G-plane crosses one of the rays R^+ or R^-. The initially small positive peak d of $\mathrm{Re}(\omega_{G1})$, occurring behind the second neutral point when we proceed along the left-hand lobe of either of the two branches to the point at infinity with $\mathrm{Re}(\omega_{G1}) \to 0$ as $k_G \to \pm 0$, continues to amplify but remains more than ten times smaller than the global maximum of $\mathrm{Re}(\omega_{G1})$ on the right-hand lobe.

Figure 4 where $m_{G0} = 0.9$ presents the evolution of these tendencies. The first dispersion curve $\omega_{G1}(k_G)$ is seen to pass entirely in the right half-plane of the complex ω_G-plane. Stable as well as neutral oscillations cease to exist after the two points on the imaginary axis determining critical frequencies merge into a single one. Simultaneously the loop disappears from the shape of the lower and upper branches of $\omega_{G1}(k_G)$. The local peak d takes the appearance of a tiny kink with m_{G0} increasing and soon becomes smoothed out from the rounded-off tips of both branches. A graph of $\omega_{G1}(k_G)$ typical of the range of large spanwise wavenumbers is computed in figure 5 with $m_{G0} = 3.0$. An increase in m_{G0} causes the global maximum g and local maximum l to fade away from the right-hand lobes of the lower and upper branches.

https://doi.org/10.1017/S0022112005007275 Published online by Cambridge University Press

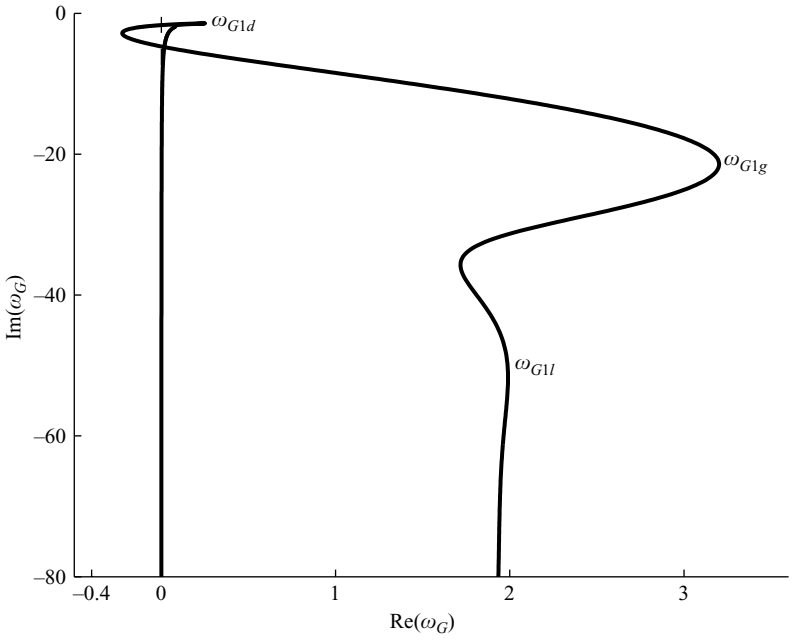


FIGURE 3. Complex ω_G-plane for $m_{G0} = 0.5$ and $M_\infty = 0$. The local positive peak d of $\mathrm{Re}(\omega_{G1})$ is a distinctive feature of the first dispersion curve.

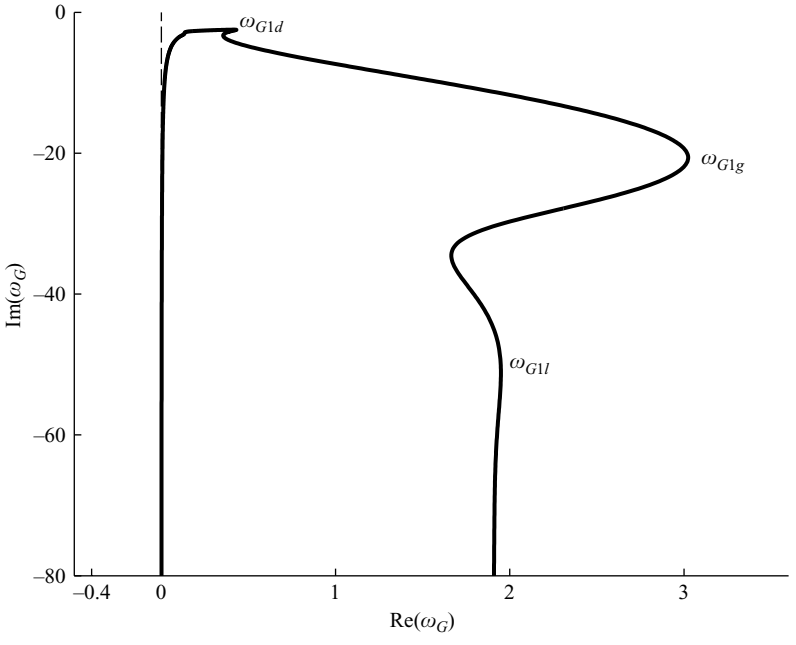


FIGURE 4. Complex ω_G-plane for $m_{G0} = 0.9$ and $M_\infty = 0$. The local positive peak d of $\mathrm{Re}(\omega_{G1})$ disappears from the first dispersion curve.

6. Compressible flows

Consider now the general case of subsonic boundary layers with an arbitrary value of the Mach number $M_\infty < 1$. Our main concern will be with the limit as $M_\infty \to 1$.

https://doi.org/10.1017/S0022112005007275 Published online by Cambridge University Press

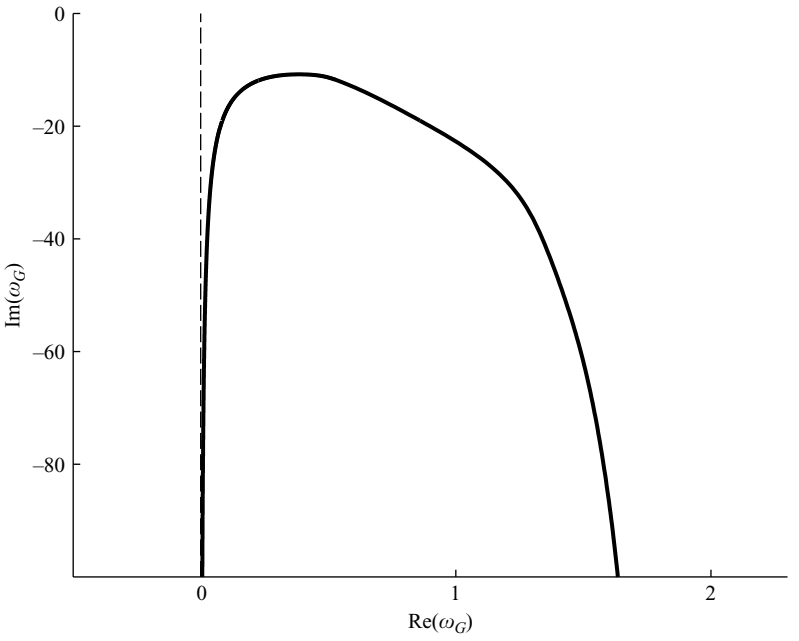


FIGURE 5. Complex ω_G-plane for $m_{G0} = 3$ and $M_\infty = 0$. All positive maxima of $\mathrm{Re}(\omega_{G1})$ fade away from both segments of the two branches of the first dispersion curve.

Alterations to the shape of the first dispersion curves are significant as the Mach number undergoes an increase from zero to unity. However, with small and moderate values of the lateral wavenumber the general behaviour of the curves still bears a close resemblance to that typical of $M_\infty = 0$. Figure 6 drawn for $m_{G0} = 0.5$ and $M_\infty = 0.98$ illustrates this statement.

A distinction between the curves in figures 3 and 6 relates mainly to the magnitude $\max_g[\mathrm{Re}(\omega_{G1})]$ of the global maximum g. It increases from 3.21 to 3.92 with the Mach number growing from 0 to 0.98. At the same time, the magnitude $\max_d[\mathrm{Re}(\omega_{G1})]$ of the local peak d at the tip of a loop incorporated into either of the two branches of the first dispersion curve remains almost unchanged, an approximate estimate being $\max_d[\mathrm{Re}(\omega_{G1})] = 0.24$ regardless of the Mach number. The frequency interval of stable oscillations becomes broader for higher values of the Mach number.

The shape of the first dispersion curves significantly changes on moving to the larger values of the lateral wavenumber. Whereas the curve in figure 4 plotted for $m_{G0} = 0.9$ and $M_\infty = 0$ has no portion in the left half-plane and no loop in the form of both branches located in the right half-plane of the complex ω_G-plane, the dispersion curve in figure 7 drawn with the same $m_{G0} = 0.9$ and $M_\infty = 0.98$ possesses these two distinctive features. Therefore, stable oscillations appear in the spectrum of swirling waves when we enter the transonic regime. Most importantly, the local peak d emerges to crown the loop. The magnitude $\max_g[\mathrm{Re}(\omega_{G1})]$ of the global maximum g increases substantially from 2.83 to 4.66, and a fairly accurate estimate $\max_d[\mathrm{Re}(\omega_{G1})] = 0.4$ holds for the local peak d as the Mach number approaches unity.

At even greater values of the lateral wavenumber, the alterations to the shape of the first dispersion curves occur more slowly. However, when the Mach number approachesly unity, perceptible changes are observed in the curves with equal m_{G0} (not shown). Instead of having a rounded-off joint of two lobes included in both

https://doi.org/10.1017/S0022112005007275 Published online by Cambridge University Press

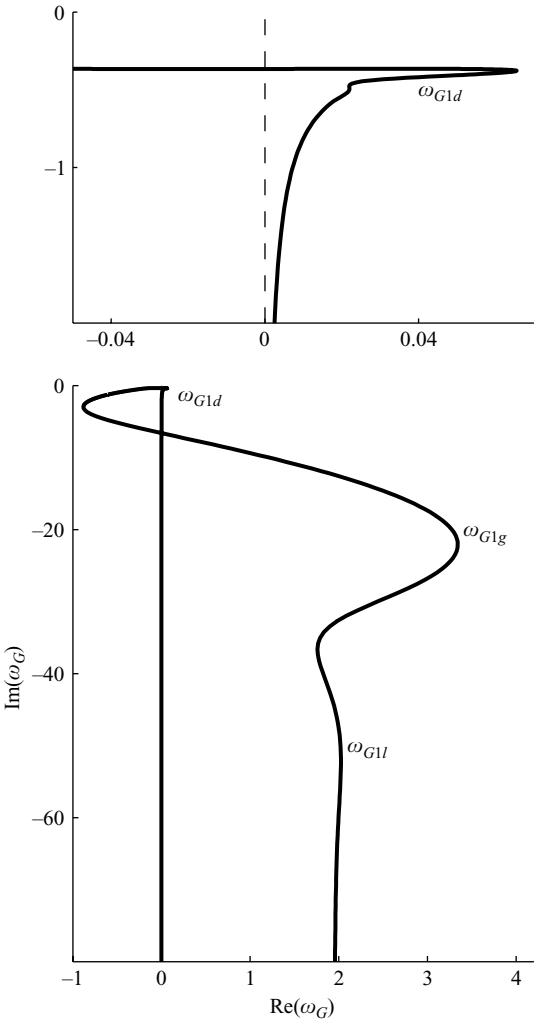


FIGURE 6. Complex ω_G-plane for $m_{G0} = 0.5$ and $M_\infty = 0.98$. For small and moderate values of the spanwise wavenumber the first dispersion curve varies slightly with the Mach number increasing to 1.

branches making up the first dispersion curve for $m_{G0} = 3.0$ in figure 5, a loop with the local peak d at its tip reappears in the vicinity of the origin and is at the basis of the wave/vortex eigenmodes' interaction. The magnitude $\max_d[\mathrm{Re}(\omega_{G1})]$ is as much as 1.05. The interval of stable oscillations becomes appreciable. Thus, the loop crowned with the sharp peak d proves to be a common characteristic of the first dispersion curves at M_∞ close to 1.

7. Convective and streamwise absolute instabilities

For all $M_\infty < 1$, the occurrence of the small local peak d in the domain where the left-hand and right-hand lobes of each branch merge together has a profound consequence for the behaviour of unstable disturbances periodic in the lateral

https://doi.org/10.1017/S0022112005007275 Published online by Cambridge University Press

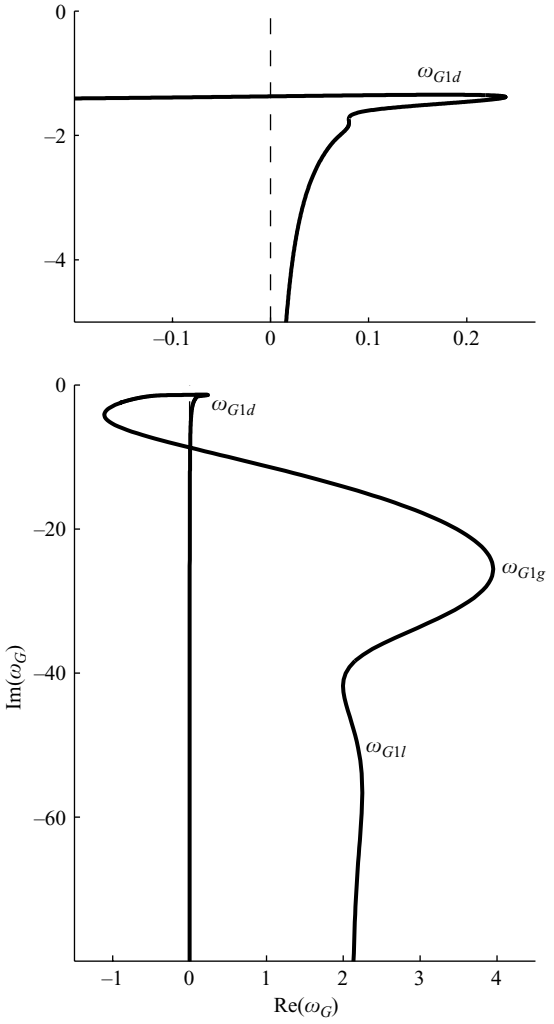


FIGURE 7. Complex ω_G-plane for $m_{G0} = 0.9$ and $M_\infty = 0.98$. A loop with a local positive peak d of $\mathrm{Re}(\omega_{G1})$ reappears in the vicinity of the origin.

direction. It follows from the general concepts of physics (see for instance Landau & Lifshitz 1959) that positive maxima attained by the real part of the complex frequency are responsible for the wave-packet generation in any viscous shear flows. This property was recently exploited by Ryzhov & Terent'ev (1998) to compute the vigorous amplification of modulated signals in a three-dimensional boundary layer with crossflow. Owing to the fact that wave packets are the most enhancing disturbances, they are of particular importance in predicting different kinds of boundary-layer instabilities to swirling waves on a concave surface. To be specific, compare the wave packets associated with the global maximum g and the local maximum l of $\mathrm{Re}[\omega_{G1}(k_G)]$ on the right-hand lobe to that induced by the small positive peak d in the domain where the left-hand and right-hand lobes merge to make up either the lower or the upper branch of the first dispersion curve. Since $\mathrm{dRe}[\omega_{G1}(k_G)]/\mathrm{d}k_G = 0$ at the extremal points we may introduce the group velocities V_g, V_l and V_d defined

https://doi.org/10.1017/S0022112005007275 Published online by Cambridge University Press

through

$$V = -\frac{\mathrm{d}\,\mathrm{Im}\,[\omega_{G1}(k_G)]}{\mathrm{d}k_G} = -\frac{\mathrm{d}\,\mathrm{Im}\,[\omega_{G1}(k_G, m_{G0})]}{\mathrm{d}k_G} \tag{7.1}$$

and labelled with the same subscripts g, l and d. Notice that the definition in (7.1) where the dependence on M_∞ and D_G is omitted relates to highly modulated disturbances with a fixed value m_{G0} of the lateral wavenumber. As mentioned above, the derivative $\mathrm{d}\,\mathrm{Im}[\omega_{G1}(k_G)]/\mathrm{d}k_G$ is negative at each point of the right-hand lobes, therefore both $V_g > 0$ and $V_l > 0$ like the phase velocity of Tollmien–Schlichting harmonic waves. Unstable monochromatic wave trains as well as wave packets induced by the global maximum g and the local maximum l underlie the conventional route to transition triggered by convective instability. In this scenario, linear and then nonlinear amplification leading to transition takes place downstream of a perturbing agency.

On the other hand, it follows from figures 2, 3, 6 and 7 that the negative sign of $\mathrm{d}\,\mathrm{Im}[\omega_{G1}(k_G)]/\mathrm{d}k_G$ changes to the positive sign when passing through the local peak d at the tip of the loop. In compliance with the observation on the sign of V_d, we may anticipate that any z-periodic perturbing source installed on a concave surface is capable of emitting, in the pulse mode, the modulated signals advancing upstream. Since $\max_d[\mathrm{Re}(\omega_{G1})]$ is more than ten times less than $\max_g[\mathrm{Re}(\omega_{G1})]$ for the case illustrated in figures 3 and 6, the amplitude of the disturbance upstream of the perturbing agency might be expected to be much weaker than the amplitude of the wave packets sweeping downstream. We emphasize at this point that the oscillation pattern in front of the exciting source is strongly influenced by the contribution from positive values of $\mathrm{Re}(\omega_{G1})$ along the left-hand lobes with $\mathrm{d}\,\mathrm{Im}(\omega_{G1})/\mathrm{d}k_G > 0$ varying monotonically. Hence the signal penetrating upstream is not a classical wave packet that depends only on an immediate vicinity of $\max_d[\mathrm{Re}(\omega_{G1})]$. The continuous contribution from the left-hand lobes becomes more significant in the case illustrated by figure 4 where $m_{G0} = 0.9$, $M_\infty = 0$ and the local peak d tends to disappear from the shape of the first dispersion curve. However, with the Mach number reaching a large subsonic value $M_\infty = 0.98$ the local peak d reappears in the form of the loop close to the origin in figure 7 and the role of this peak in inducing weak wave packets upstream substantially increases. With the lateral wavenumber m_{G0} increased to 3.0, no points with extremal values of $\mathrm{Re}(\omega_{G1})$ are seen in the first dispersion curve drawn in figure 5 for $M_\infty = 0$. Accordingly, a single disturbance pattern moving as a whole downstream and with long-scaled pulsation cycles in the upstream direction might be reasonably predicted to be brought about by the continuous variations of $\mathrm{Re}(\omega_{G1}) > 0$ and $\mathrm{d}\,\mathrm{Im}(\omega_{G1})/\mathrm{d}k_G$, both negative and positive.

The signals of all the types under discussion grow exponentially fast. Hence we are led to introduce the concept of absolute instability in the streamwise direction as applied to the two-dimensional boundary layer on a concave surface. This concept, as distinct from the absolute instability proper (Huerre & Monkewitz 1990; Brevdo 1991), has been put forward by Lingwood (1997) and Ryzhov & Terent'ev (1998) in studies of the initially three-dimensional boundary layer with crossflow on a swept wing. They coined a new term to emphasize the essence of the matter that disturbances from a point source are absolutely unstable in the chordwise direction on the wing surface but free to drift in the spanwise direction. The well-organized z-periodic structures of Görtler vortices recorded in wind-tunnel tests (Saric 1994)

https://doi.org/10.1017/S0022112005007275 Published online by Cambridge University Press

seem to be more relevant to the transition process on a concave surface, compared to a point-impulse excitation.

A model to be tested experimentally for demonstrating centrifugal instability in the boundary-layer flow should have a concave insert downstream of a nearly flat portion of a wing. In the absence of absolute instability in the streamwise direction, the boundary layer on the front part of the wing surface would be impacted in the linear stage by only two-dimensional Tollmien–Schlichting waves up to the line where the concave insert sticks out of the flat plate. However, in measurements by a special single-axis three-component laser velocimeter Mangalam *et al.* (1985) observed small spanwise variations of the streamwise velocity at or just ahead of the beginning of the concave zone. The wavelength of this variation matched the observed wavelength in the downstream concave region, pointing to the vortical nature of upstream stretching disturbances. This observation provides direct evidence in support of the concept under discussion. It is worth noting that nonlinear structures resulting from the swirling waves are difficult to record in front of the concave insert installed on the wing because the magnitude of the local peak d is small and the spiral-type Görtler vortices decay without being maintained by centrifugal forces on the flat surface. For the same reason, the swirling waves are hardly detectable computationally without taking special precautions. This difficulty was obviated in Ryzhov (2003) and Ryzhov & Bogdanova-Ryzhova (2003) where large-amplitude short-scaled oscillation cycles produced by $\max_g[\mathrm{Re}(\omega_{G1})]$ are partially filtered out from downstream moving wave packets. With filtering incorporated into a numerical scheme, the difference in the amplitude of short-scaled and long-scaled cycles is substantially reduced. In consequence, the upstream moving wave packets can be clearly seen in the computation.

8. Receptivity to surface vibrations

As a rule, the Görtler vortices are recorded in wind-tunnel tests as an array of elongated structures spaced periodically in the spanwise direction Saric (1994). Starting from this observation, let us consider a simple receptivity problem where disturbances are assumed to be induced by a vibrating ribbon brought into operation in a pulse mode. Since impulsively excited wave packets have the spectrum of frequencies which necessarily contains the most amplified linear modes, they may be envisioned as disturbances vigorously building up in time and space.

Initial-boundary-value problem

Guided by these preliminary remarks, we concentrate in the subsequent analysis on wave systems emitted during the initial pulse motion of the ribbon. To attain this goal, the ribbon is specified by

$$y = y_w = \begin{cases} a\sin(\omega_0 t)\, f(x)\cos(m_0 z), & t \geqslant 0, \\ 0, & t < 0, \end{cases} \tag{8.1}$$

with a function f being effectively non-zero only within a finite interval. The perturbing agency amplitude is fixed by a parameter a which is assumed to be small. When applied to the Görtler spectral side band, f should be transformed by means of

$$f \to \varepsilon^{-3/7}(\overline{\kappa} D)^{-1/7} f_G(x_G). \tag{8.2}$$

https://doi.org/10.1017/S0022112005007275 Published online by Cambridge University Press

As a result the ribbon shape

$$y_G = y_{Gw} = \begin{cases} a \sin(\omega_{G0} t_G)\, f_G(x_G) \cos(m_{G0} z_G), & t_G \geqslant 0, \\ 0, & t_G < 0 \end{cases} \tag{8.3}$$

remains invariant.

The no-slip conditions

$$u = w = 0, \tag{8.4a}$$

$$v = \frac{\partial y_w}{\partial t} \tag{8.4b}$$

at the moving wall with $y = y_w(t, x, z)$ given in (8.1) replace (3.10). In the receptivity problem posed, it is natural to choose as initial data

$$u = w = 0 \qquad \text{at } t = 0 \tag{8.5}$$

in order to observe the birth and subsequent development of various types of disturbances.

The Prandtl equations (3.5*a–c*) supplemented with the interaction law (3.11) and subjected to the limit conditions (3.9*a*, *b*) as well as the boundary conditions (8.4*a*, *b*) are linearized by using (4.1) with the small parameter a prescribing the ribbon vibration swing. According to the discussion in § 5, the resulting linear problem is well posed.

With allowance made for (4.1) and (8.1), the no-slip conditions (8.4*a*, *b*) reduce to

$$(\tilde{u}, \tilde{v}, \tilde{w}) = [-\sin(\omega_0 t), \omega_0 \cos(\omega_0 t), 0] f(x) \mathrm{Re}(\mathrm{e}^{\mathrm{i}m_0 z}) \text{ at } y = 0, t \geqslant 0. \tag{8.6}$$

In line with (8.6), a solution is sought in the form

$$(\tilde{u}, \tilde{v}, \tilde{w}, \tilde{p}, \tilde{A}) = \mathrm{Re}[(u_c, v_c, w_c, p_c, A_c)\mathrm{e}^{\mathrm{i}m_0 z}]. \tag{8.7}$$

As distinct from (4.2), here the desired complex-valued functions u_c, v_c, w_c, p_c, A_c are transformed into the Laplace integral in t to accommodate the initial data (8.5) and the Fourier integral in x by means of

$$[\overline{u}_c(\omega, k, y), \overline{v}_c(\omega, k, y), \overline{w}_c(\omega, k, y), \overline{p}_c(\omega, k), \overline{A}_c(\omega, k)]$$
$$= \int_{-\infty}^{\infty} \mathrm{d}x \int_0^{\infty} \mathrm{e}^{-(\omega t + \mathrm{i}kx)} [u_c(t, x, y), v_c(t, x, y), w_c(t, x, y), p_c(t, x), A_c(t, x)] \mathrm{d}t. \tag{8.8}$$

Substitution of (8.7) and (8.8) into the system of linearized Prandtl equations leaves us with a set of ordinary differential equations (4.3*a–c*) for the function-images $\overline{u}_c$, $\overline{v}_c$, $\overline{w}_c$, $\overline{p}_c$, $\overline{A}_c$ if the initial data for $\tilde{u}$ and $\tilde{w}$ are zero. The limit conditions (4.4*a*, *b*) at infinity and the interaction law cast in (4.5) remain intact. The no-slip conditions become

$$(\overline{u}_c, \overline{v}_c, \overline{w}_c) = (-1, \omega, 0)\, \overline{f}(k)\, \frac{\omega_0}{\omega^2 + \omega_0^2} \qquad \text{at } y = 0 \tag{8.9}$$

where $\overline{f}(k)$ is a Fourier transform of the vibrator shape $f(x)$. With $f(x)$ assumed below to be an even function, the Fourier transform $\overline{f}(k)$ is real.

With (8.9) substituted for homogeneous conditions (4.6), we can easily formulate a boundary-value problem for $F = k\overline{u}_c + m_0 \overline{w}_c$. Notice that F may be regarded as an asymptotic representation, as $Re \to \infty$, of the normal Orr–Sommerfeld mode both in the Tollmien–Schlichting spectral range and the vortical Görtler side band.

https://doi.org/10.1017/S0022112005007275 Published online by Cambridge University Press

Pressure disturbances

In what follows, we confine ourselves to the analysis and computation of the pressure variations using an explicit representation

$$p_c = \frac{\omega_0 \mathrm{i}}{4\pi^2} \int_{-\infty}^{\infty} \mathrm{d}k \mathrm{e}^{\mathrm{i}kx} \overline{f}\,(k) \left\{ k^2 \left[k^2 + \left(1 - M_\infty^2\right)^{-1} m_0^2 \right]^{-1/2} + \varepsilon^3 \overline{\kappa} D \right\} \times J\,(t, k; \omega_0, m_0; M_\infty, \varepsilon, \overline{\kappa} D)\,, \quad (8.10a)$$

$$J = \int_{L-\mathrm{i}\infty}^{L+\mathrm{i}\infty} \mathrm{d}\omega \mathrm{e}^{\omega t} \frac{\Phi\,(\Omega)}{\left(\omega^2 + \omega_0^2\right) \left[\Phi\,(\Omega) - Q\,(k, m_0; M_\infty, \varepsilon, \overline{\kappa} D)\right]} \quad (8.10b)$$

that is derivable in a straightforward way from a solution of the boundary-value problem posed for F. With the dispersion-relation properties clarified in § 5, we may proceed to calculating the wave systems both downstream and upstream of the ribbon by utilizing a technique developed by Ryzhov & Terent'ev (1998). Since a continuous part is missing from the ω-spectrum for all real k, both positive and negative, let us expand the inverse Laplace transform (8.10*b*) entering the right-hand side of (8.10*a*) into series in residues of the integrand at its poles. Finally, we are left with a simplified expression

$$p_{cG} = -\frac{\mathrm{i}^{2/3} \omega_{G0}}{2\pi} \int_{-\infty}^{\infty} \mathrm{d}k_G \mathrm{e}^{\omega_{G1}(k_G) t_G + \mathrm{i} k_G x_G} \overline{f}_G\,(k_G) \times \left\{ \frac{k_G^2}{\left[D_G k_G^2 + \left(1 - M_\infty^2\right)^{-1} m_{G0}^2 \right]^{1/2}} + 1 \right\} \frac{k_G^{2/3} \mathrm{dAi}\,(\Omega_{G1})/\mathrm{d}Y}{\left[\omega_{G1}^2\,(k_G) + \omega_{G0}^2\right] \mathrm{Ai}\,(\Omega_{G1}) \left[\Omega_{G1} + \Phi\,(\Omega_{G1})\right]} \quad (8.11)$$

to evaluate the pressure in the wave-packet oscillation cycles. Here a transformation from the triple-deck to Görtler variables has been used to identify the disturbances called into being by the left-hand lobes with $\mathrm{d}\,\mathrm{Im}(\omega_{G1})/\mathrm{d}k_G > 0$ which are incorporated into both branches of the first dispersion curve.

Wave packets

Computed results are in full accord with the inferences from the general analysis of spectral properties intrinsic to modulated disturbances both in the Tollmien–Schlichting wave range and the Görtler vortex side band. They clearly demonstrate the importance of the vortex spacing and Mach number in determining the pulsation systems emitted by the ribbon. Our purpose is to trace the changes in the disturbance pattern related to typical forms of the first dispersion curves in figures 3–7 as the spanwise wavenumber increases from 0.5 to 3.0 while the Mach number rises from 0 to a high subsonic value 0.98.

The global maximum g and the small positive peak d of $\mathrm{Re}(\omega_{G1})$ are the 'silent' features of the dispersion curves in figures 3 and 6 where $m_{G0} = 0.5$. Both curves relate to a range of vortex spacing that leads to a well-defined loop in the form of either of their branches. Since the curves are very much alike, the pressure variations associated with this value of m_{G0} are displayed in figure 8 for $M_\infty = 0$ only. The results computed substantiate theoretical predictions from the general concepts of physics that have been made in § 7. Accordingly, the global maximum induces short-scaled pulsation cycles in the wave packet moving downstream, in compliance with the conventional scenario of convective instability. The local peak d in the dispersion-relation loop underlies much longer pulsation cycles in the signal advancing in the region upstream of the vibrating ribbon, contrarty to traditional notions of hydrodynamic stability theory. Similar disturbances have been discovered by Ryzhov & Terent'ev (1998) in

https://doi.org/10.1017/S0022112005007275 Published online by Cambridge University Press

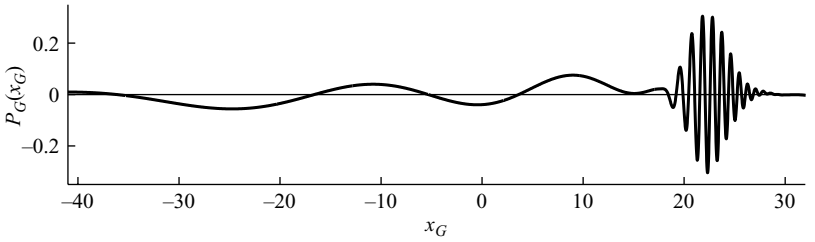


FIGURE 8. Wave system for $m_{G0} = 0.5$, $M_\infty = 0$ and $t_G = 12.0$. Two distinct wave packets propagate both downstream and upstream, the latter provoking absolute instability in the streamwise direction.

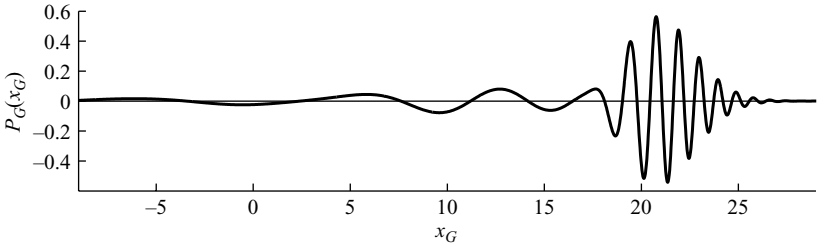


FIGURE 9. Wave system for $m_{G0} = 0.9$, $M_\infty = 0$ and $t_G = 12.0$. A weak upstream advancing signal is produced by the continuous contribution from positive $\mathrm{Re}(\omega_{G1})$ along the entire length of the left-hand lobes.

the three-dimensional boundary layer with crossflow. The oscillation pattern in the upstream penetrating signal was found to be strongly influenced by a continuous distribution of positive $\mathrm{Re}(\omega_{G1})$ over some portions of the left-hand lobes with $\mathrm{d}\,\mathrm{Im}(\omega_{G1})/\mathrm{d}k_G > 0$ that are incorporated into both branches of the first dispersion curve. Hence, the signal in front of the vibrating ribbon emerges not as a classical wave packet depending on an immediate vicinity of $\max_d[\mathrm{Re}(\omega_{G1})]$, but rather the amplitude of its pulsation cycles decays very slowly as x_G takes on large negative values. Then, $\max_d[\mathrm{Re}(\omega_{G1})]$ is more than ten times smaller than $\max_g[\mathrm{Re}(\omega_{G1})]$, therefore the maximum swing in the highly modulated wave packet that sweeps downstream would exceed the size of the upstream penetrating signal by several orders in magnitude at $t_G = 10{-}15$ if no special technique has been used in the computation. Since our interest at this point focuses on the oscillation pattern advancing upstream of a perturbing source, the short-scaled cycles in the downstream moving wave packet produced by $\max_g[\mathrm{Re}(\omega_{G1})]$ were partially filtered out when computing the pressure distributions in figure 8 shown on a representative scale. Otherwise, the upstream stretching pulsation structure could not be displayed on a single plot with the highly modulated disturbance behind the ribbon. Similar plots using representative scales are exhibited in other figures below to trace the disturbance development with time.

The disturbance pattern computed with $m_{G0} = 0.9$ and $M_\infty = 0$ is drawn in figure 9. The role of the tiny kink with $\max_d[\mathrm{Re}(\omega_{G1})]$ in the first dispersion curve, as was discussed in connection with figure 4, becomes negligible in inducing oscillations in front of the perturbing source. Here the continuous contribution from positive $\mathrm{Re}(\omega_{G1})$ along the left-hand lobes with $\mathrm{d}\,\mathrm{Im}(\omega_{G1})/\mathrm{d}k_G > 0$ becomes of crucial importance. On the other hand, $\max_g[\mathrm{Re}(\omega_{G1})]$ stands out sharply in the form of the right-hand lobes with $\mathrm{d}\,\mathrm{Im}(\omega_{G1})/\mathrm{d}k_G < 0$. As a consequence, the size of the long-scaled oscillation

https://doi.org/10.1017/S0022112005007275 Published online by Cambridge University Press

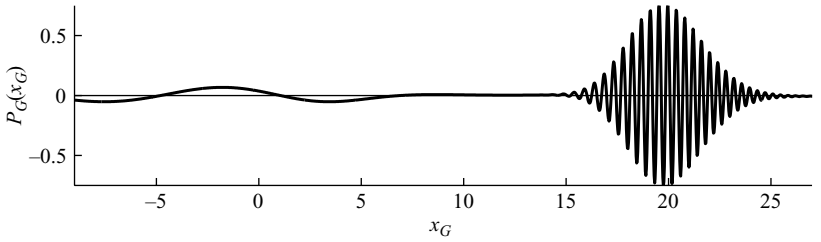


FIGURE 10. Wave system for $m_{G0} = 0.9$, $M_\infty = 0.98$ and $t_G = 9.0$. Disruption of oscillation cycles into two signals is due to the reappearance of the local positive peak d of $\mathrm{Re}(\omega_{G1})$ in the first dispersion curve.

cycles upstream of the vibrating ribbon is small, whereas the downstream moving disturbance still arises as a classical highly modulated wave packet, notwithstanding the fact that short-scaled pulsations are partially damped out in the computation.

Let us turn to the high subsonic Mach number regime specified by the same value $m_{G0} = 0.9$ and $M_\infty = 0.98$. As follows from the plot of the first dispersion curve in figure 7, the loop with the local peak d of $\mathrm{Re}(\omega_{G1})$ reappears in both branches close to the origin. Hence the contribution from the immediate vicinity of d to the pulsation system ahead of the ribbon might reasonably be expected to increase somewhat. The wave pattern presented in figure 10 substantiates this prediction. The upstream moving disturbances separate from the downstream sweeping wave packet, slowly build up and gradually generate a weakly modulated signal. Disruption of the oscillation system into two parts with a short interval of almost uniform motion in between occurs because of a large portion of the loop in the half-plane $\mathrm{Re}(\omega_G) < 0$ that causes amplitude damping.

Drastic alterations to the wave pattern that propagates in the incompressible boundary layer come about, with m_{G0} attaining a value as large as 3.0. The evolution of a single disturbance with time and space can be observed in figure 11 with longer-scaled cycles extending far upstream. This structure was predicted in § 7 on the basis of simple arguments that all the points with positive extrema of $\mathrm{Re}(\omega_{G1})$ disappear from the left-hand and right-hand lobes of the first dispersion curve. Thus, the signal in figure 11 is produced entirely by the contribution from these lobes with variations of $\mathrm{d}\,\mathrm{Im}(\omega_G)/\mathrm{d}k_G$ continuously changing from negative to positive. As a result, the single wave system is equally responsible for the conventional scenario of convective instability and a new type of absolute instability in the streamwise direction. As has been already mentioned, the points with extrema of $\mathrm{Re}(\omega_{G1})$ are re-established in the shape of the first dispersion curve, and a loop again emerges to connect its left-hand and right-hand lobes as $M_\infty \to 1$. Disruption of the wave pattern into two modulated signals takes place in a manner similar to that in figure 10. The downstream moving wave packet triggers the conventional path to convective instability whereas the upstream advancing oscillation cycles provoke absolute instability in the streamwise direction.

9. Discussion and conclusions

As a rule, the interaction of Tollmien–Schlichting waves and Görtler vortex eigenmodes has long been considered by assuming the disturbance amplitude to exceed a certain threshold value, thereby switching on weakly or truly nonlinear amplification mechanisms. For sufficiently large pulsations, the mean-flow profile

https://doi.org/10.1017/S0022112005007275 Published online by Cambridge University Press

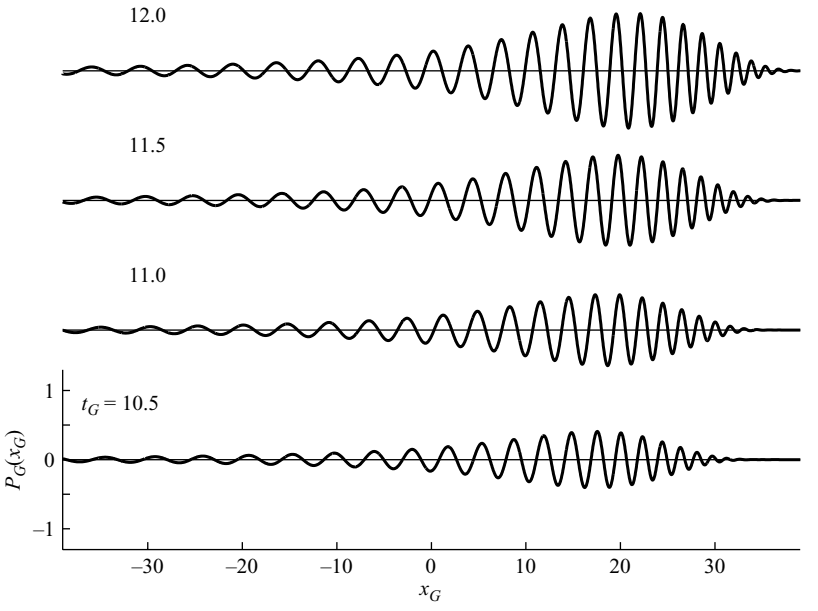


FIGURE 11. The evolution of a wave pattern computed with $m_{G0} = 3.0$ and $M_\infty = 0$ and various t_G. Signals of this type underlie equally the conventional route to convective instability as well as absolute instability in the streamwise direction.

throughout the boundary layer is completely altered from its initial unperturbed state. Under these circumstances, interacting oblique Tollmien–Schlichting waves can generate longitudinal vortices very much akin to Görtler vortices even in the absence of wall curvature. The strongly nonlinear interactions also include the possibility of a finite-distance break-up in the spatially developing flow, owing to a singularity in the instantaneous displacement thickness. A thorough study of these distinctive properties can be found in Hall & Smith (1988, 1989, 1991) and references therein.

At approximately the same time Timoshin (1990) and Denier *et al.* (1991) independently identified five different asymptotic regimes intrinsic to Görtler vortical periodic structures depending on the vortex spacing. The triple-deck disturbance pattern underlies one of them, controlled by the viscous/inviscid interaction typical of many boundary-layer flows. A set of governing equations without time-dependent terms turns out to be identical to that derived earlier by Rozhko & Ruban (1987) and applied by Rozhko *et al.* (1988) to the steady boundary layer on a body with an elongated obstacle placed on its curved surface. With time-dependence included, Ruban (1990*a*, *b*) and Choudhari *et al.* (1994) attacked the receptivity problem on the wave packet emitted by a vibrator operating in the pulse mode.

A composite asymptotic model developed in § 3 for large Reynolds numbers covers both the Tollmien–Schlichting wave and Görtler vortex disturbances coupled together through the interaction law (3.11) that specifies the self-induced pressure variations in the system of governing Prandtl equations (3.5*a–c*). Unlike the high Reynolds number descriptions adopted in Hall & Smith (1988, 1989, 1991), the model involves the wave/vortex interaction even within the framework of a linear approach due to the fact that there exists a domain in the spectral space where the eigenmodes of both

https://doi.org/10.1017/S0022112005007275 Published online by Cambridge University Press

types overlap. As a result, the frequencies and wavenumbers inherent in Tollmien–Schlichting waves form the base spectrum and those specific to Görtler vortices give rise to a side band where the interaction law (3.11) reduces to its simplified version (3.17) by Rozhko & Ruban (1987) and the streamwise pressure gradient drops out of the Prandtl equations. However, in the overlapping domain of the spectral space, all the eigen-frequencies and wavenumbers are scaled and normalized according to (4.13*a–c*) and (5.1*a–c*) that makes both terms in the braces in (4.11) of equal order in magnitude for typical transition conditions.

Unusual behaviour of the first dispersion curves in the auxiliary Ω_G-plane and in the plane of complex frequencies is a direct consequence of the wave/vortex eigenmodes' coupling in the linear stage of amplification. As has been shown in §§ 5 and 6, the first dispersion curve divides into two separate branches in the ω_G-plane and each of the branches consists of two segments associated either with the Tollmien–Schlichting wave or Görtler vortex eigenmodes. With moderate values of the spanwise wavenumber, the loop connecting both segments arises from the eigenmodes' interaction. A kink at the tip of the loop underlies the radiation of upstream propagating wave packets.

The wave packets propagating downstream in figures 8–10 illustrate the development of convective instability in boundary layers on a concave surface due to an exponential increase of the pressure variation swing. This type of disturbance amplification is known to be fundamental to conventional routes to transition in two-dimensional shear flows not affected by centrifugal forces, the Blasius boundary layer on a flat plate being the simplest example. With the surface curvature not zero, centrifugal forces come into play; however, the contribution from the Görtler vortex side band to the downstream sweeping wave packet is negligibly small as dictated by the $O(\varepsilon^3)$-correction term in the interaction law (3.11).

On the other hand, computed results introduce oscillation systems advancing against the oncoming stream. It should be emphasized that the computed systems belong among the disturbances developing most violently in the streamwise direction of an incompressible boundary layer and high subsonic Mach number flows. To a marked extent they are controlled by the local maximum d of $\mathrm{Re}(\omega_{G1})$ on the loop of the dispersion curves in figures 3, 6 and 7. Signals of this kind result in the initial flow field breakdown ahead of a perturbing source that operates in the pulse mode. They are responsible for the streamwise absolute instability of a steady boundary layer on a concave surface.

The oscillation pattern exhibited in figure 11 for closely spaced vortices ($m_{G0} = 3.0$) in the incompressible boundary layer gives an example of a single modulated signal excited by a ribbon. As predicted, the signal moves downstream as a whole, but long-scaled pulsation cycles at its rear extend far upstream. The reason is that all positive extrema of $\mathrm{Re}(\omega_{G1})$ fade away from the shape of the first dispersion curve in figure 5. The oscillation pattern under consideration provokes equally the conventional path to convective instability as well as absolute instability in the streamwise direction.

The first evidence for the existence of absolutely unstable oscillations in flows acted upon by centrifugal forces came to light in a related study of a rotating disk by Lingwood (1995). She advanced, using the pinching criterion from the work of Briggs (1964) and Bers (1975) in plasma physics, theoretical arguments establishing the concept of absolute instability and then substantiated her analysis by direct measurements. Apparently, the axial structure of the excited velocity field in the experimental investigation by Lingwood (1996) was of the type exhibited in figure 11, where a single disturbance consists of pulsation cycles stretching both upstream and

https://doi.org/10.1017/S0022112005007275 Published online by Cambridge University Press

downstream. The position at which the disturbance trailing edge comes to rest on the disk is identified with the laminar boundary-layer breakdown and the onset of transition. However, the rotating-disk flow is strictly periodic in the circumferential direction, hence only the radial component of the group-velocity vector has to vanish for absolute instability to become operative.

Until very recently, there was a good consensus of opinion that the rotating-disk flow can serve as a pertinent model for the swept-wing boundary layer. A closer look at the problem led Lingwood (1997) and Ryzhov & Terent'ev (1998) to introduce the new concept of streamwise absolute instability. They started from a periodic formulation assuming the initial perturbation to derive from a ribbon aligned with crossflow. Under these conditions, the group-velocity vector points in the direction of the local outer stream. Note however that the two studies cover different intervals of frequencies and wavenumbers.

The spanwise-periodic formulation given in (8.1) or (8.3) above is closely related to that in Ryzhov & Terent'ev (1998) assuming the Reynolds number to be large enough. The study focuses on the streamwise absolute instabilitiy leaving aside the issue of absolute instability proper (Huerre & Monkewitz 1990; Brevdo 1991). The formulation is dictated by the fact that the well-organized z-periodic structures are experimentally known to arise in boundary layers on a concave surface (Saric 1994). Therefore, the assumption of a point-impulse excitation would not lead to an adequate theoretical problem. The constraints imposed allow us to deal with a single inverse Fourier transform (8.11) in the Görtler spectral range in order to compute the low-amplitude long-scaled oscillation cycles in the wave packets advancing upstream of the ribbon. From a purely mathematical point of view, a multiplier $k^{-5/3}$ or $k_G^{-5/3}$, entering, respectively, expressions (4.11) or (5.2), on the right-hand side of the dispersion relation (4.10) lies at the heart of streamwise absolute instability in a two-dimensional boundary layer on a concave surface. An analogous singularity features a three-dimensional boundary layer with crossflow and renders it absolutely unstable in the streamwise direction Ryzhov & Terent'ev (1998). It is the denominator of Q which causes the first dispersion curve in the complex frequency plane to divide into two symmetrically located branches, each of which consists of two different lobes merging together as shown in figure 2 for small values of the spanwise wavenumber. The left-hand lobes are missing from the shape of the first dispersion curve in the particular case of two-dimensional disturbances with $m_{G0} = 0$. Both right-hand lobes carry negative values of $\mathrm{d}\,\mathrm{Im}(\omega_{G1})/\mathrm{d}k_G$ whilst the same derivative has positive values along the left-hand lobes. Therefore, the two right-hand lobes trigger convective instability as is well-known from numerous studies. On the other hand, the two left-hand lobes are associated with absolutely unstable disturbances capable of advancing upstream from the periodically shaped ribbon. Disturbances of this kind originate in the boundary layer on a concave surface from coupling of travelling waves with unsteady Görtler vortices.

Both left-hand lobes may be treated as creating a specific viscous eigenmode in the plane of complex frequencies. Apparently, an analogous but spatially damped inviscid mode has been identified by Mack (1985) and Balakumar & Malik (1990) in connection with the rotating-disk boundary layer. The new mode briefly mentioned by them is central to the analysis in Lingwood (1995). Note that the behaviour of the eigenmode comprising both left-hand lobes of the first dispersion curve becomes intricate in the plane of complex wavenumbers because it has branch-point singularities and cuts (Ryzhov & Terent'ev 1986).

https://doi.org/10.1017/S0022112005007275 Published online by Cambridge University Press

A streaky pattern at the front edge of the disturbance can be evaluated starting from the Kelvin stationary-phase principle on condition that $|x_G/t_G| \gg 1$. The structure acquired by the signal with small values of the surface curvature $\overline{\kappa}$ is of special interest. Thus, the original triple-deck variables should be substituted into a relation that derives from the Kelvin principle applied to an integral in (8.11). As a result, we have

$$p = -\frac{\omega_0}{(2\pi)^{1/2}} D_G^{21/32} \overline{f}(k_{ph}) \, |m_0|^{-1/2} \, \frac{t^{3/4}}{(-x)^{5/4}} \cos(m_0 z) \tag{9.1}$$

where $\overline{f}(k_{ph})$ is real with the vibrator shape $f(x)$ prescribed by an even function. A stationary-phase wavenumber

$$k_{ph}^2 = D_G^{1/8} m_0^2 \frac{t}{(-x)}$$

exists provided that the streamwise coordinate x takes on negative values in the region upstream of a vibrator. Clearly, this is a standing wave with amplitude algebraically growing in time and decaying to zero with upstream distance from the pulsed ribbon. On the strength of (5.3), we may infer from (9.1) that the upstream propagation vanishes when the Reynolds number tends to infinity and/or the surface curvature becomes infinitely small.

A comment is due now on the basic solution

$$u = y, \quad v = w = p = A = 0 \tag{9.2}$$

of the Prandtl equations with the self-induced pressure gradiant included that was used in (4.1) to develop a linear approach. As is evident from the foregoing, this solution does not represent a physically realizable boundary layer as a final steady state. The spanwise-periodic disturbances exponentially grow at every point in space and strongly affect the velocity field. Neither the basic state (9.2) nor the exponentially amplifying disturbances can be recorded experimentally. A value of the spanwise wavenumber m_0 is likely to be forced through the nonlinear selectivity mechanisms of different mode amplification that triggers the primary stationary vortex pattern on a concave surface. From the theory advanced, the primary vortex pattern may be predicted to extend upstream, thereby offering a clue to putting to the test the concept of streamwise absolute instability. Experimental evidence for the upstream influence exerted by the Görtler vortex structure is traced back to Mangalam *et al.* (1985) where "...velocity measurements indicated small spanwise variation at or just ahead of the beginning of the concave zone". This direct observation is at variance with the conventional stability results because no streamwise vortices can start developing on a flat portion of the surface located in front of a concave insert. Indeed, if the Görtler vortices in Mangalam *et al.* (1985) were caused by the mechanism of convective instability, they would require some distance from the leading edge of the concave insert to enhance to a measurable size. Convectively unstable disturbances would be swept downstream without giving rise to spanwise variation in front of the concave insert on an otherwise flat plate.

The subsequent growth of primary Görtler vortices is controlled by the linear centrifugal instability up to a position on the concave surface where strong nonlinear mechanisms come into operation (Hall & Smith 1988, 1989, 1991). Secondary travelling-wave-type disturbances in the form of sinuous and varicose eigenmodes start developing and completely modify the initial velocity field. These secondary instabilities eventually provoke the breakdown of the laminar boundary layer at

https://doi.org/10.1017/S0022112005007275 Published online by Cambridge University Press

some stage prior to transition (Li & Malik 1995; Bottaro & Klingmann 1996). It is worth noting that a similar mechanism controls the primary crossflow vortices (Koch 2002; Saric *et al.* 2003). Transition to turbulence in a swept-wing boundary layer occurs farther downstream as a result of secondary instabilities of a great many nonlinearly interacting modes coming into play only above a certain threshold amplitude of the primary crossflow vortex pattern. It is vital to note that in general the secondary instability properties need not be the same as those intrinsic to the primary instability. In fact, all secondary instabilities discovered so far seem to be of convective nature (Koch 2002; Wassermann & Kloker 2002; Saric *et al.* 2003). Hence the streamwise absolute instability of primary vortices does not necessarily mean earlier transition. On the contrary, this opens up new intriguing possibilities for flow control by artificially exciting the primary vortices with lower receptivity to external perturbations and/or small growth rates of secondary instabilities. Instead of hastening transition, the secondary vortices may delay the onset of random pulsations.

The authors are indebted to all of the referees for their remarks and suggestions. The work of O.S.R. was sponsored by the Air Force Office of Scientific Research, Air Force Material Commands, USAF under grant #F49620-03-1-0043 and monitored by Dr. A. Nachman.

REFERENCES

Abramowitz, M. & Stegun, I. A. 1964 *Handbook of Mathematical Functions*. National Bureau of Standards.

Balakumar, P. & Malik, M. R. 1990 Travelling disturbances in rotating-disk flow. *Theor. Comput. Fluid Dyn.* **2**, 125–137.

Bers, A. 1975 Linear waves and instabilities. In *Physique de Plasmas* (ed. C. Dewitt & J. Peyraud), pp. 117–215. Gordon & Beach.

Bodonyi, R. J. & Smith, F. T. 1981 The upper branch stability of the Blasius boundary layer, including nonparallel flow effects. *Proc. R. Soc. Lond.* A **375**, 65–98.

Bottaro, A. & Klingmann, B. G. B. 1996 On the linear breakdown of Görtler vortices. *Eur. J. Mech.* B/*Fluids* **15**, 301–330.

Brevdo, L. 1991 Three-dimensional absolute and convective instabilities, and spatially amplifying waves in parallel shear flows. *Z. Angew. Math. Phys.* **42**, 911–942.

Briggs, R. J. 1964 *Electron-Stream Interaction with Plasmas*. MIT Press.

Choudhari, M., Hall, P. & Streett, C. 1994 On the spatial evolution of long-wavelength Görtler vortices governed by a viscous-inviscid interaction. Part I: The linear case. *Q. J. Mech. Appl. Maths.* **47**, 207–229.

Coles, D. 1965 Transition in circular Couette flow. *J. Fluid Mech.* **21**, 385–425.

Comte, P. & David, E. 1996 Large-eddy simulation of Görtler vortices in a curved compression ramp. In *Experimentation, Modelling and Computation in Flow, Turbulence and Combustion*, Vol. 1, pp. 45–61. J. Wiley & Sons.

Denier, J. P., Hall, P. & Seddougui, S. O. 1991 On the receptivity problem for Görtler vortices: vortex motions induced by wall roughness. *Phil. Trans. R. Soc. Lond.* A **335**, 51–85.

Floryan, J. M. 1991 On the Görtler instability of boundary layers. *Prog. Aerosp. Sci.* **28**, 235–271.

Görtler, H. 1940 Über den Einfluss der Wandkrümmung auf die Entstehung der Turbulenz. *Z. Angew. Math. Mech.* **20**, 138–147.

Görtler, H. 1955 Dreidimensionale Instabilität der ebenen Staupunktströmung gegenüber wirbelartigen Störungen. In *Fünfzig Jahre Grenzschichtforschung*, pp. 304–314. Vieweg Verlag.

Hall, P. 1982 Taylor-Görtler vortices in fully developed or boundary layer flows: linear theory. *J. Fluid Mech.* **124**, 475–494.

Hall, P. 1983 The linear development of Görtler vortices in growing boundary layers. *J. Fluid Mech.* **130**, 41–58.

https://doi.org/10.1017/S0022112005007275 Published online by Cambridge University Press

Hall, P. 1990 Görtler vortices in growing boundary layers: The leading edge receptivity problem, linear growth, and nonlinear breakdown stage. *Mathematika* **37**, 151–189.

Hall, P. & Smith, F. T. 1988 The nonlinear interaction of Tollmien–Schlichting waves and Taylor-Görtler vortices in curved channel flows. *Proc. R. Soc. Lond.* A **417**, 255–282.

Hall, P. & Smith, F. T. 1989 Nonlinear Tollmien–Schlichting wave/vortex interaction in boundary layers. *Eur. J. Mech.* B/*Fluids* **8**, 179–205.

Hall, P. & Smith, F. T. 1991 On strongly nonlinear vortex/wave interactions in boundary-layer transition. *J. Fluid Mech.* **227**, 641–666.

Huerre, P. & Monkewitz, P. A. 1990 Local and global instabilities in spatially developing flows. *Annu. Rev. Fluid Mech.* **22**, 473–537.

Koch, W. 2002 On the spatio-temporal stability of primary and secondary crossflow vortices in a three-dimensional boundary layer. *J. Fluid Mech.* **456**, 85–111.

Landau, L. D. & Lifshitz, E. M. 1959 *Fluid Mechanics*. Pergamon.

Li, F. & Malik, M. R. 1995 Fundamental and subharmonic secondary instabilities of Görtler vortices *J. Fluid Mech.* **297**, 77–100.

Lingwood, R. J. 1995 Absolute instability of the boundary layer on a rotating disk. *J. Fluid Mech.* **299**, 17–33.

Lingwood, R. J. 1996 An experimental study of absolute instability of the rotating disk boundary-layer flow. *J. Fluid Mech.* **314**, 373–405.

Lingwood, R. J. 1997 On the impulse response for swept boundary-layer flows. *J. Fluid Mech.* **344**, 317–344.

Mack, L. M. 1985 The wave pattern produced by point source on a rotating disk. *AIAA Paper* 85-0490.

Mangalam, S. M., Dagenhart, J. R., Hepner, T. E. & Meyers, J. F. 1985 The Görtler instability on an airfoil. *AIAA Paper* 85-0491.

Rayleigh, Lord 1880 On the stability, or instability, of certain fluid motions. *Proc. Lond. Math. Soc.* **11**, 57–70.

Rayleigh, Lord 1916 On the dynamics of revolving fluid. *Proc. R. Soc. Lond.* A **93**, 148–154.

Ruban, A. I. 1990*a* Propagation of wave packets in the boundary layer on a curved surface. In *Proc. IUTAM Symp. Laminar-Turbulent Transition* (ed. D. Armal & R. Michel), pp. 103–111. Springer.

Ruban, A. I. 1990*b* Propagation of wave packets in the boundary layer on a curved surface. *Izv. Akad. Nauk SSSR, Mekh. Zhidk. Gaza*, No. 2, 59–68 (in Russian; English translation: *Fluid Dyn.* **25**, 213–221, 1990).

Rozhko, S. B. & Ruban, A. I. 1987 Longitudinal-transverse interaction in a three-dimensional boundary layer. *Izv. Akad. Nauk SSSR., Mekh. Zhidk. Gaza*, No. 3, 42–50 (in Russian; English translation: *Fluid Dyn.* **22**, 362–371, 1987).

Rozhko, S. B., Ruban, A. I. & Timoshin, S. N. 1988 Interaction of a three-dimensional boundary layer with an elongated obstacle. *Izv. Akad. Nauk SSSR, Mekh. Zhidk.* Gaza, No. 1, 39–48 (in Russian; English translation: Fluid Dyn. **23**, 30–37, 1988).

Ryzhov, O. S. 1980 Unsteady three-dimensional boundary layer freely interacting with an external stream. *Prikl. Matem. Mekhan.* **44**, 1035–1052 (in Russian; English translation: *PMM USSR* **44**, 739–750, 1982).

Ryzhov, O. S. 2003 Advances in hydrodynamic stability theory: the wave/vortex eigenmodes' interaction. In *Numerical Simulations of Incompressible Flows*. World Scientific.

Ryzhov, O. S. & Bogdanova-Ryzhova, E. V. 2003 Boundary layer instabilities in transonic range of velocities. In *Proc. IUTAM Symp. Transsonicum IV*. Kluwer.

Ryzhov, O. S. & Terent'ev, E. D. 1986 On the transition mode characterizing the triggering of a vibrator in the subsonic boundary layer on a plate. *Prikl. Matem. Mekhan.* **50**, 974–986 (in Russian; English translation: *PMM USSR*, **50**, 753–762, 1987).

Ryzhov, O. S. & Terent'ev, E. D. 1998 Streamwise absolute instability of a three-dimensional boundary layer at high Reynolds numbers. *J. Fluid Mech.* **373**, 111–153.

Saric, W. S. 1994 Görtler vortices. *Annu. Rev. Fluid Mech.* **26**, 379–409.

Saric, W. S., Reed, H. L. & White, E. B. 2003 Stability and transition of three-dimensional boundary layers. *Annu. Rev. Fluid Mech.* **35**, 413–440.

Schmid, P. J. & Henningson, D. S. 2001 *Stability and Transition in Shear Flows*. Springer.

https://doi.org/10.1017/S0022112005007275 Published online by Cambridge University Press

Smith, F. T. 1979 On the non-parallel flow stability of the Blasius boundary layer. *Proc. R. Soc. Lond.* A **366**, 91–109.

Smith, F. T. 1982 On high Reynolds number theory of laminar flows. *IMA J. Appl. Maths* **28**, 207–281.

Smith, F. T., Sykes, R. I. & Brighton, P. W. 1977 A two-dimensional boundary layer encountering a three-dimensional hump. *J. Fluid Mech.* **83**, 163–176.

Smith, F. T. & Walton, A. G. 1989 Nonlinear interaction of near-planar TS waves and longitudinal vortices in boundary-layer transition. *Mathematika* **36**, 262–289.

Squire, H. B. 1933 On the stability of three-dimensional disturbances of viscous fluid flow between parallel walls. *Proc. R. Soc. Lond.* A **142**, 621–628.

Stewartson, K. 1974 Multistructured boundary layers on flat plates and related bodies. *Adv. App. Mech.* **14**, 145–239.

Taylor, G. I. 1921 Experiments with rotating fluids. *Proc. Camb. Phil. Soc.* **20**, 326–329.

Taylor, G. I. 1923 Stability of a viscous liquid contained between two rotating cylinders. *Phil. Trans. R. Soc. Lond.* A **223**, 289–343.

Taylor, G. I. 1935 Distribution of velocity and temperature between concentric rotating cylinders. *Proc. R. Soc. Lond.* A **151**, 494–512.

Terent'ev, E. D. 1984 The linear problem on a vibrator performing harmonic oscillations at supercritical frequencies in a subsonic boundary layer. *Prikl. Matem. Mekhan.* **48**, 264–272 (in Russian; English translation: *PMM USSR* **48**, 184–191, 1984).

Terent'ev, E. D. 1985 Linear problem on vibrator on a flat plate in subsonic boundary layer. In *Proc. IUTAM Symp. Laminar-Turbulent Transition*. Springer.

Timoshin, S. N. 1990 Asymptotic analysis of a spatially unstable Görtler vortex spectrum. *Izv. Akad. Nauk SSSR, Mekh. Zhidk. Gaza*, No. 1, 32–41 (in Russian; English translation: *Fluid Dyn.* **25**, 18–25, 1990).

Walton, A. G. & Smith, F. T. 1992 Properties of strongly nonlinear vortex/Tollmien–Schlichting wave interaction. *J. Fluid Mech.* **244**, 79–100.

Wasow, W. 1965 *Asymptotic Expansions for Ordinary Differential Equations*. John Wiley and Sons.

Wassermann, P. & Kloker, M. 2002 Mechanisms and passive control of crossflow-vortex-induced transition in a three-dimensional boundary layer. *J. Fluid Mech.* **456**, 49–84.

https://doi.org/10.1017/S0022112005007275 Published online by Cambridge University Press